ELECTRON INTERFEROMETRY USING AN AMPLITUDE DIVIDING GRATING BEAMSPLITTER: DEVELOPMENT AND APPLICATION

by

FEHMI SAMI YASIN

A DISSERTATION

Presented to the Department of Physics
and the Graduate School of the University of Oregon
in partial fulfillment of the requirements
for the degree of
Doctor of Philosophy

June 2019

DISSERTATION APPROVAL PAGE

Student: Fehmi Sami Yasin

Title: Electron Interferometry Using an Amplitude Dividing Grating Beamsplitter: Development and Application

This dissertation has been accepted and approved in partial fulfillment of the requirements for the Doctor of Philosophy degree in the Department of Physics by:

Benjamín Alemán	Chair
Benjamin J. McMorrran	Advisor
Michael Raymer	Core Member
Brad Nolen	Institutional Representative

and

Janet Woodruff-Borden	Dean of the Graduate School

Original approval signatures are on file with the University of Oregon Graduate School.

Degree awarded June 2019

DISSERTATION ABSTRACT

Fehmi Sami Yasin

Doctor of Philosophy

Department of Physics

June 2019

Title: Electron Interferometry Using an Amplitude Dividing Grating Beamsplitter: Development and Application

Electron microscopes can be used for atomic resolution imaging myriad materials including semiconductor nanomaterials integral to modern technology, biomolecular materials that compose all of life and the carbon energy cycle, and 2-D materials with various potential applications. Due to the high electron dose required to form contrast in conventional electron microscopy imaging techniques, many biomolecular and low atomic number materials are destroyed before an image can be formed. Electron interferometry shows promise as a lower dose imaging technique due to the difference in how contrast is formed. Electron holography, for example, uses an electrostatic charged wire as an electron biprism in order to overlap the interaction and vacuum electron waves to form interference fringes. These fringes can be imaged directly and processed to measure the object transmission function, providing both spatial information such as atomic locations, and quantitative phase and amplitude information, necessary for thickness and electric and magnetic field measurement within the specimen. In this work, we combine electron holography with Scanning Transmission Electron Microscopy (STEM), which forms a focussed probe beam at the specimen and raster scans the beam over a field of view. We've experimentally realized a path-separated electron interferometer in this mode, called STEM holography (STEMH), and apply it to image gold nanoparticles on thin amorphous carbon at subnanometer resolution. STEMH simultaneously forms efficient, interpretable contrast for both of these materials, allowing us to confirm the presence of string-like structure within the amorphous carbon, previously thought to be randomly bonded and oriented. Additionally, we've devised and implemented a multi-biprism design that enables tuning of the path separation between the arms of the interferometer at the specimen plane, and we demonstrate the largest path-separated amplitude division electron interferometer to date. This flexible STEMH enables large geometry experiments and a means to precisely place the probes in the specimen plane, enabling imaging around beam-sensitive materials and probing fundamental physical phenomena in or around materials. On its own, STEMH can probe fundamental fields with atomic resolution, and advances in detector technology may allow STEMH to image beam-sensitive materials without destroying them in the process.

This dissertation includes previously published co-authored material.

CURRICULUM VITAE

NAME OF AUTHOR: Fehmi Sami Yasin

GRADUATE AND UNDERGRADUATE SCHOOLS ATTENDED:
University of Oregon, Eugene
Westminster College, Salt Lake City, UT

DEGREES AWARDED:
Doctor of Philosophy, Physics, 2019, University of Oregon
Bachelor of Science, Physics, 2013, Westminster College

AREAS OF SPECIAL INTEREST:
Electron Interferometry
Phase-Contrast Scanning Transmission Electron Microscopy
Scanning Transmission Electron Microscope Holography

PROFESSIONAL EXPERIENCE:

NSF Graduate Research Opportunities Worldwide Fellow, Center for Exploratory Research, Hitachi, Ltd., Hatoyama, Saitama, JAPAN, 2017-2018

NSF Graduate Research Fellow, University of Oregon, 2015-2018

Science Literacy Program Fellow, University of Oregon, 2015

Graduate Research Assistant, University of Oregon, 2014-2015

Graduate Teaching Fellow, University of Oregon, 2013-2015

GRANTS, AWARDS AND HONORS:

Microscopy Society of America Travel Scholarship Award, International Congress of Microscopy 19, 2018

Special "opps" Travel and Research Award, International Congress of Microscopy 19, 2018

National Science Foundation Graduate Research Opportunities Worldwide Fellowship, 2017

Microscopy and Microanalysis Meeting Student Scholar Award, Microscopy and Microanalysis Meeting, 2016

Graduate Teaching Fellowship, UO Science Literacy Program, Spring 2015

Graduate Teaching Fellowship, UO Science Literacy Program, Winter 2015

National Science Foundation Graduate Research Fellowship, 2015

Weiser Senior Teaching Assistant Award, UO Department of Physics, 2015

PUBLICATIONS:

TR Harvey, **FS Yasin**, JJ Chess, JS Pierce, RMS dos Reis, VB Özdöl, P Ercius, J Ciston, W Feng, NA Kotov, BJ McMorran, C Ophus. *Phys. Rev. Appl.*, 2018, **10**, 6, 061001

FS Yasin, K Harada, D Shindo, H Shinada, BJ McMorran, T Tanigaki. *Appl. Phys. Lett.*, 2018, **113**, 233102

FS Yasin, TR Harvey, J Chess, JS Pierce, C Ophus, P Ercius, BJ McMorran. *Nano Lett.* 2018, **18**, 11, 7118-7123

BJ McMorran, TR Harvey, C Ophus, J Pierce, **FS Yasin**. *Microsc. Microanal.* 2018, **24**, S1, 200-201

TR Harvey, V Grillo, F Venturi, JS Pierce, **FS Yasin**, JJ Chess, S Frabboni, E Karimi, BJ McMorran. *Microsc. Microanal.* 2018, **24**, S1, 938-939

FS Yasin, TR Harvey, J Chess, JS Pierce, BJ McMorran. *J. Phys. D: Appl. Phys.*, 2018, **51**, 205104

J Ziegler, A Blaikie, A Fathalizadeh, D Miller, **FS Yasin**, K Williams, J Mohrhardt, BJ McMorran, A Zettl, B Alemán. *Nano Lett.* 2018, **18**, 4, 2683-2688

FS Yasin, TR Harvey, JJ Chess, JS Pierce, BJ McMorran. *Microsc. Microanal.* 2016, **22**, 506

CW Warren, DW Miller, **FS Yasin**, JT Heath. *2013 IEEE 39th Photovoltaic Specialists Conference (PVSC).* 2013, 0170-0173

TABLE OF CONTENTS

Chapter Page

LIST OF FIGURES

CHAPTER I

INTRODUCTION

In 1887, Michelson demonstrated a practical light interferometer, paving the way for applications ranging from imaging of transparent phase objects [1], to fundamental quantum measurements [2], to the recent gravitational wave detections [3]. Since Dennis Gabor proposed an "electron interference microscope" in 1948 [4], electron interferometry has also been utilized for nanometer to atomic resolution imaging applications and to probe fundamental physics. Because electrons and photons both exist as particle-wave phenomena, they may be used in such interferometric setups to great effect. Electrons, however, offer several differences from their optical counterparts. Electrons are massive, charged and have a shorter De Broglie wavelength than photons. Yet they can still accelerate to relativistic speeds, and their charge enables them to interact strongly with electromagnetic fields. Their picometer wavelength provides electron interferometers with higher resolving power, making them important tools for exploring fundamental physics and materials research.

Electron interferometers were first built in 1953 by Marton *et al.* using amplitude-dividing polycrystalline epitaxially grown copper membrane diffraction gratings [5]. Möllenstedt and Düker developed the more versatile wavefront-dividing electron biprisms in 1955 [6], enabling the development of electron holography, now a trusted technique for quantitative high precision imaging [7, 8, 9, 10, 11] and probing basic physics [12, 13, 14]. While electron biprisms have proven a dependable beam-splitting technology, they have a few drawbacks when compared to amplitude-dividing beamsplitters. These include strict demands on the illuminating electron beam coherence width, assymetry in the output beams' profile and Fresnel diffraction phenomena associated with the edges of the biprism [15].

Another consideration is whether to configure the beam into a wide, transmission electron microscopy (TEM) mode, or the focussed-probe, scanning TEM (STEM) mode within the microscope. In conventional off-axis TEM holography, an electron biprism is placed in an image plane of the specimen. It must be placed in a vacuum region parallel to the edge of the specimen and engaged to overlap a vacuum reference wave with the interaction wave to form interference fringes. These fringes are then imaged directly on a charge-coupled device (CCD) camera. This setup limits sample geometries to those with an easily available vacuum region near the edge of the specimen large enough to contain a biprism within the field of view. Alternatively, STEM holography employs a pre-specimen beamsplitter, and the optics are configured to focus the multiple, spatially separated beams down to probes at the specimen. Such a setup was theorized and experimentally attempted in three groups simultaneously in the late 1980s/ early 1990s [16, 17, 18, 19]. Ultimately, detector and biprism technology at the time limited the practicality of such an interferometer, and it was set aside.

In 2014, conversations with my advisor Benjamin McMorran and colleagues Tyler Harvey, Jordan Chess and Jordan Pierce lead to a push for me to develop a path-separated STEM interferometer using amplitude-dividing nanofabricated diffraction gratings that have been used as phase plates within the McMorran lab since its creation in 2011 [20, 21]. After achieving the promising preliminary results presented in Chapter I of this dissertation, we discovered the aforementioned literature and Tyler, Jordan and I pushed to change the name of the technique to STEM holography (STEMH) as an homage to its history. My advisor still argues that the word ‘interferometry’ is technically more accurate. While presenting the results at a conference, Toshiaki Tanigaki of Hitachi, Ltd. Research and Development Group suggested that we combine wavefront-dividing electron biprisms with STEMH. Together we discovered that this would enable a tunable path-separated electron interferometer with all of the coherence-width advantages of the STEMH experimental setup mentioned above but with the added flexibility of pushing the interferometer’s paths further apart or closer together, enabling more flexibility in experimental setups. We therefore coapplied for the National Science Foundation Graduate Research Opportunities Worldwide (GROW) fellowship in order to build such an interferometer.

Simultaneously, realizing that the detector technology severely limited STEMH in the past, we employed the technique in the TEAM I at the National Center for Electron Microscopy (NCEM) at Lawrence Berkeley National Lab in Berkeley, California, a Thermo Fisher Titan 80/300 kV (S)TEM equipped with both probe and image correction as well as a Gatan Summit K2 fast-readout detector. The K2 is a direct electron detector, meaning that it is sensitive to single electron events and therefore requires less dose to acquire a high signal-to-noise interference fringe pattern. This collaboration resulted in the first demonstration of STEMH at atomic resolution, presented in Chapter III.

Following this demonstration, we were notified that I received the GROW fellowship and was to be named a Japanese Society for the Promotion of Science (JSPS) international research fellow beginning in the Fall of 2017. Upon arrival at Hitachi, Ltd. Center for Exploratory Research in Hatoyama, Saitama, Japan, Dr. Tanigaki and I installed a diffraction grating into a Hitachi TEM containing five electron biprisms. I built a scanning mode for the microscope and by Christmas, we acheived our first STEMH images. The following year we finished developing flexible STEMH, presented in Chapter IV.

This dissertation consists of work from five previously published papers. I have chosen to include three of the previously published papers that I am first author of, organized into three chapters. These chapters describe our historical development of STEMH, starting with our initial proof-of-principle demonstration, a model of the interferomter output, and an experimental comparison to the model. The next chapter describes a technique to extract measured phase shifts from the interference fringe patterns and demonstrates an application of this to an atomic resolution quantitative phase and amplitude imaging technique. The final chapter describes our development of an electron interferometer with tunable path separation. Each chapter suggests applications of this new tool, such as capabilities for probing physics within nanomaterials and measuring electric and magnetic nano-fields.

The following manuscripts are included in this work:

Chapter II. Initial Development and Theory

Fehmi S. Yasin, Tyler R. Harvey, Jordan J. Chess, Jordan S. Pierce, and Benjamin J. Mcmorran. "Path-separated electron interferometry in a scanning transmission electron microscope." *Journal of Physics D: Applied Physics* **51** 205104 (2018).

Chapter III. Application

Fehmi S. Yasin, Tyler R. Harvey, Jordan J. Chess, Jordan S. Pierce, Colin Ophus, Peter Ercius, and Benjamin J. Mcmorran. "Probing Light Atoms at Subnanometer Resolution: Realization of Scanning Transmission Electron Microscope Holography." *Nano Letters* **18** (11) 7118-7123 (2018).

Chapter IV. Further Development

Fehmi S. Yasin, Ken Harada, Daisuke Shindo, Hiroyuki Shinada, Benjamin J. Mcmorran, and Toshiaki Tanigaki. “A tunable path-separated electron interferometer with an amplitude-dividing grating beamsplitter.” *Applied Physics Letters* **113** 233102 (2018).

This work was partially supported by the U.S. Department of Energy, Office of Science, Basic Energy Sciences, under Award DE-SC0010466 and by the National Science Foundation Graduate Research Fellowship Program under grant No. 1309047. F.S.Y. is a JSPS International Research Fellow.

CHAPTER II

DEVELOPMENT

Note on ‘Path-separated electron interferometry in a scanning transmission electron microscope’

Reprinted (adapted) with permission from Fehmi S Yasin *et al.* *Journal of Physics D: Applied Physics* **51**, 205104 (2018). Copyright 2018 IOP PUBLISHING, LTD.

Benjamin McMorran conceived of the idea, and he and I developed the experimental plan. Tyler Harvey showed me how to use the electron microscope and we performed the first experimental attempt together. I performed the experiment from which the published data was collected, and Tyler and I developed the theory independently, making different approximations but meeting regularly to discuss and integrate our ideas. Tyler developed the final generalized theory inspired by [22] that we used to develop the phase reconstruction software. Tyler and I developed the software in python, meeting regularly with Jordan Chess to optimize the code. Jordan Chess and Jordan Pierce both contributed to the theoretical development as well through regular meetings where they offered advice and experience integral to developing a final working product. Jordan Pierce fabricated the diffraction gratings used in the experiment. I performed the STEMH simulations with the advice and guidance of Tyler and Jordan C.. I recorded experimental data, analyzed the experimental and simulated data, produced all figures, and wrote the supplemental material and manuscript with input from co-authors.

Introduction to Path-separated electron interferometry in a scanning transmission electron microscope

Since Michelson's practical demonstrations of interferometry in 1887, interferometric techniques have been used in optics for a great variety of applications, from fundamental quantum measurements [2], to gravitational wave sensing [3], to imaging of transparent objects [1]. Using the wave-like characteristics of light, interferometers split a beam of light into two or more paths that then recombine to form an interference pattern. If one path acquires a phase shift relative to the other, for example by passing through an object, then the resulting phase can be measured by a modification in the interference pattern. In a Mach-Zehnder interferometer, shown schematically in Fig. 1a, the interference pattern is typically measured using a second beamsplitter to analyze the interference that occurs where the two paths overlap, but in principle the interference fringes could be imaged directly using a camera.

In 1948, Dennis Gabor proposed a variation of this setup within an electron microscope. Later called holography, Gabor hypothesized an "electron interference microscope" and demonstrated the principle within an optical setup [4]. Originally meant to overcome the difficulties posed by lens aberrations within a TEM, two new issues emerged when Haine and Mulvey [23] experimentally realized Gabor's idea: the 'twin-image problem' of in-line holography, which arises because the object and reference wave forming the interference pattern propagate in the same direction in space [11, 24, 25], and the limited extension of spatial coherence in the hologram plane. Much work has been done to remedy these issues [24, 25, 26], including the creation of 'off-axis' holography by Leith and Upatnieks [27]. Once adapted to the electron microscope, the beam was split using a Möllenstedt electron biprism [28] *after* the sample, rather than before. This solved the 'twin-image problem' because the reference wave interferes with the object wave at an angle, allowing them to be separated in Fourier space [11]. Additionally, H. Wahl overcame the limited coherence problem by recording the interference pattern (hologram) in an image plane [26]. Off-axis electron holography has since been developed and applied[9, 10, 29, 30, 31, 32] to push the boundaries of electron microscopy through feats such as the atomic resolution electrostatic potential mapping of graphene sheets [33]. Although it remains a state of the art imaging technique, off-axis electron holography uses a wavefront-division beamsplitter, which requires a wide, coherent beam, which in turn requires a highly coherent source. As stated before, this requirement can be met, but remains a non-trivial task that requires expertise. Additionally, the phase resolution is limited by the number of fringes within the field of view. Finally, the biprism has a non-trivial installation in commercial electron microscopes and creates unwanted artifacts in the interference pattern due to diffraction from the biprism's edge.

To overcome these restraints, multiple amplitude-division crystal lattice beamsplitters have been proposed and utilized by Matteucci et al.[34], Ru et al.[35], Zhou [36], Agarwal et al.[37] and others since Marton et al. first demonstrated them in 1952 [5, 38, 39]. Additionally, diffraction gratings have also been developed as amplitude-dividing beamsplitters for electrons [40, 41] and applied to electron interferometers [42, 43, 44]. Gronniger et al. had a three-grating setup which required and external laser source for alignment, while Cronin and McMorran used two gratings for a Lau [44] and Talbot [43] interferometer setup. Holographic diffraction gratings for electrons have been developed by several groups [20, 21, 45, 46, 47] to carefully design the intensity and phase structure of the probe beams. As diffraction grating fabrication techniques have improved, so has the spatial separation range of the diffracted probes.

Here we demonstrate that a single nanoscale grating can be used as a coherent beamsplitter to form a separated-path interferometer in an electron microscope. These gratings diffract the electron wavefront into probes with spatial separation of tens of nanometers under standard lens settings in commercial TEMs. This separation is sufficient to study nano-materials using classic interferometric techniques. Such a technique within an electron microscope was initially theorized and explored experimentally in the late 1980's and early 1990's [16, 18, 22]. The initial experimental attempts proved too challenging for the reasons mentioned above, and so the technique was ultimately abandoned, although Cowley expanded the theory in 2003 [48]. In this paper we experimentally explore and discuss the feasibility of his idea of "STEM holography."

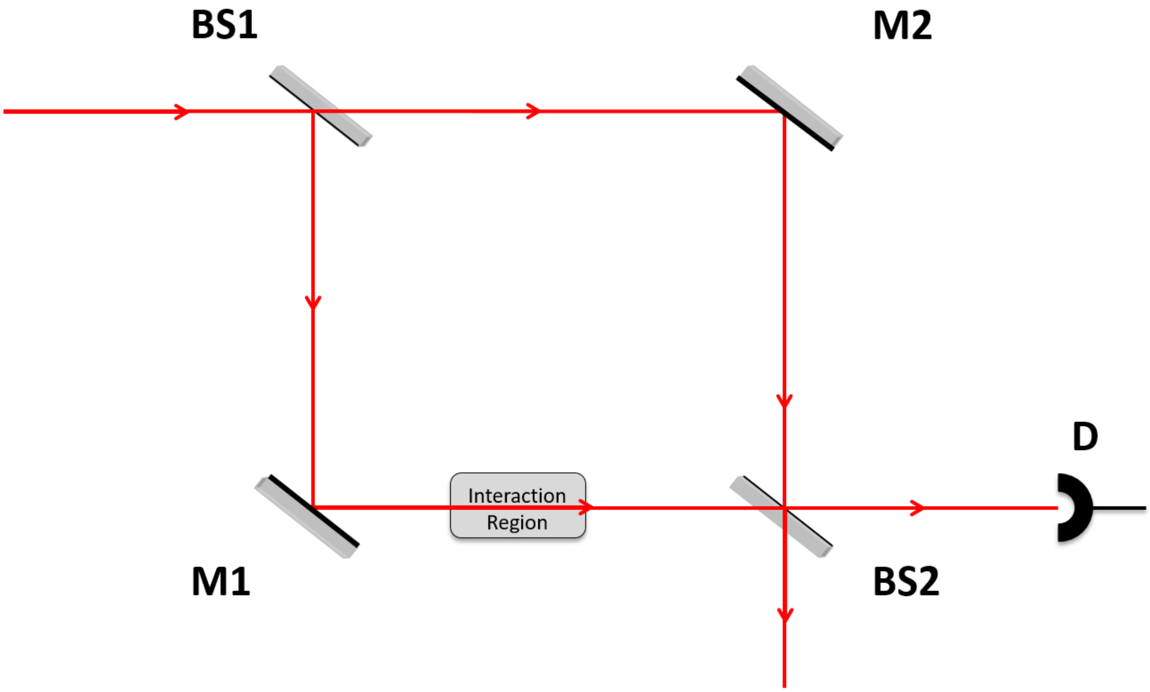

FIGURE 1. (a) Mach-Zehnder Interferometry

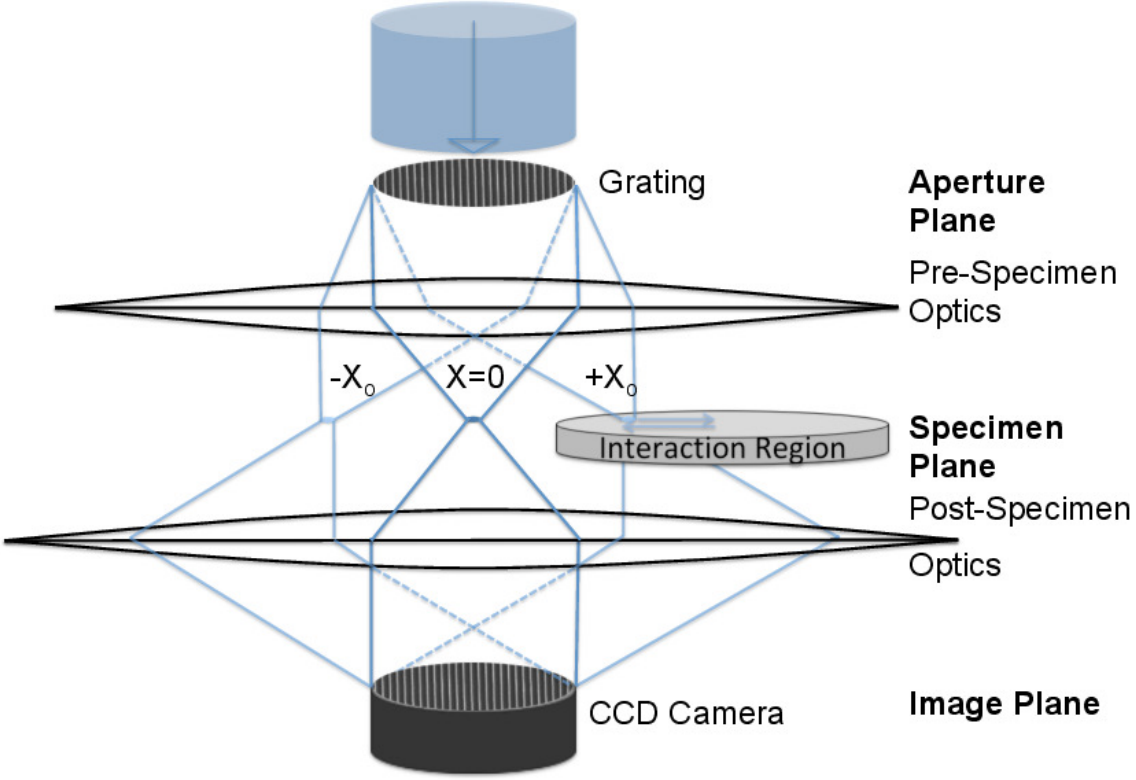

FIGURE 1. (b) Experimental setup for an analagous electron interferometer that uses a grating beamsplitter and magnetic lenses as mirrors. The electron beam is split into diffracted probes by a diffraction grating. The +1 order probe interacts with the phase-object while the 0 and -1 order probes pass through vacuum. The TEM's imaging system recombines the paths, magnifies the resulting interference pattern and projects it onto the CCD camera.

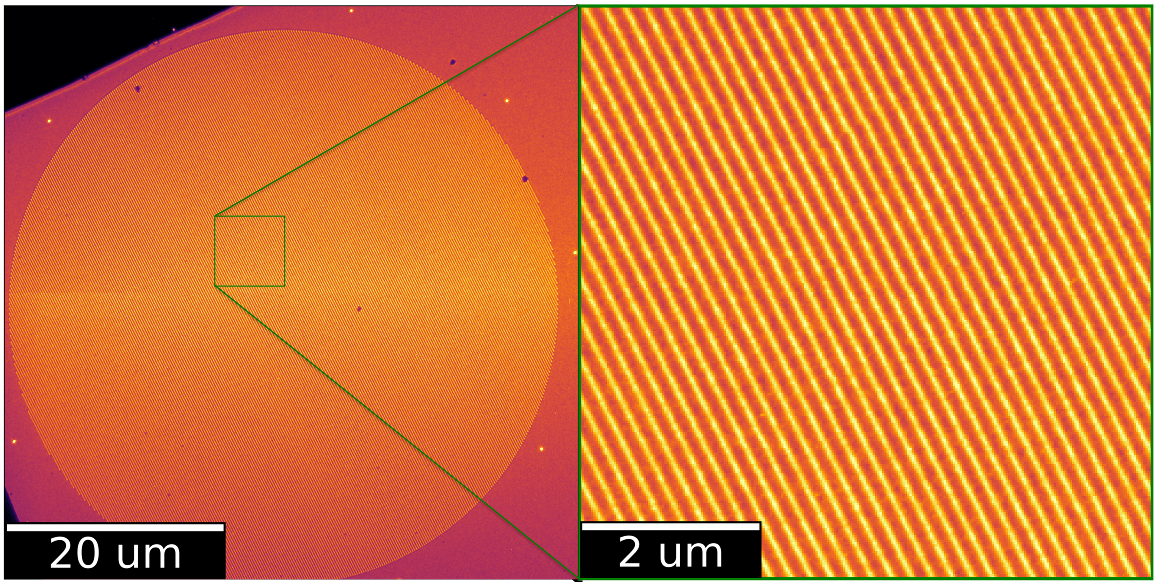

FIGURE 2. TEM image of the 50 μm diameter, 200 nm pitch sine profile diffraction grating within the condenser lens aperture. A 6.5 μm $\times$ 6.5 μm slice of the grating is shown in the green cutout.

Experimental Setup

We performed this experiment on an FEI 80-300 Titan operated at 300 keV in STEM mode. Using a Focused Ion Beam (FIB), we fabricated a 50 μm diameter, 200 nm pitch diffraction grating (shown in Fig. 2) in a Ti and Pt coated silicon nitride membrane [21]. The grating bars were milled using a 30 kV accelerating voltage, 24 pA beam of Ga ions. Once milled, the grating was positioned in the Condenser 2 aperture plane.

As illustrated in Fig. 8b, the input plane wave electron beam travels down the microscope column to the C2 aperture, where it diffracts through the grating and forms isolated electron probes at the specimen plane with tens of nanometers spatial separation (shown in Fig. 3). In this experiment, we position a phase object such that the three most intense diffraction probes initially pass through vacuum. The phase object we used was a Ted Pella Combined TEM Test Specimen on a 3 mm grid, consisting of graphitic carbon and gold nanoparticles on nearly electron-transparent amorphous carbon. The nanoparticles provide recognizable features that can be used for alignment of the diffracted probe beams, and they have a known mean inner potential that can be used to predict the phase shift imparted to transmitted electrons. The probes are then scanned across the field of view so that the +1 order probe interacts with the phase object while the 0 and -1 order probes pass through vacuum. They are then recombined through the post-specimen optics and interfere in the image plane on a Gatan Ultrascan 1000 CCD camera. An image of the grating (interference pattern) is acquired by the CCD camera at each location in the scan. The phase information at each location on the phase object may be extracted by a post process described in the theory section below. We specifically illuminated the graphitic carbon, as it provides an easily recognizable change in thickness ($\triangle z$) when the probe scans from vacuum onto the phase object.

The phase object is shown in Fig. 4a using conventional STEM High Angle Anular Dark Field (HAADF) imaging. A regular focused probe is rastered across the phase object. At each probe position, the electrons are scattered by the atoms they pass. The more atoms the beam of electrons interact with, the higher number of counts on the HAADF detector. The projection lens system is set to a camera length of 130 mm. At this camera length, a 6 mrad convergence angle corresponds to a beam radius of 0.78 mm at the phosphor screen, three times smaller than the HAADF detector's inner radius. Therefore, the HAADF signal is proportional to the thickness of the phase object, as well as the atomic number, Z [49]. Since the phase object we're considering is homogeneous, we approximate the signal to be proportional to thickness.

With the diffraction grating inserted, the electron probes were scanned from vacuum onto the edge of the carbon, along the drawn line indicated in Fig. 4a. Along each point in the scan, an image of the diffraction grating (interference fringes) was recorded and analyzed. Some of these fringes are shown in Fig. 4b, which confirms the translation of the fringes shift across the scan as expected. In addition to translation, however, we observed a doubling of the fringe frequency and a loss of contrast of the lowest spatial frequency. We explore why this occurs in the next section.

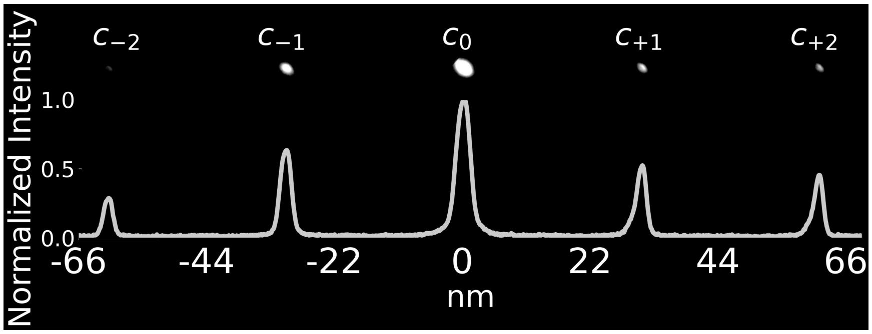

(a)

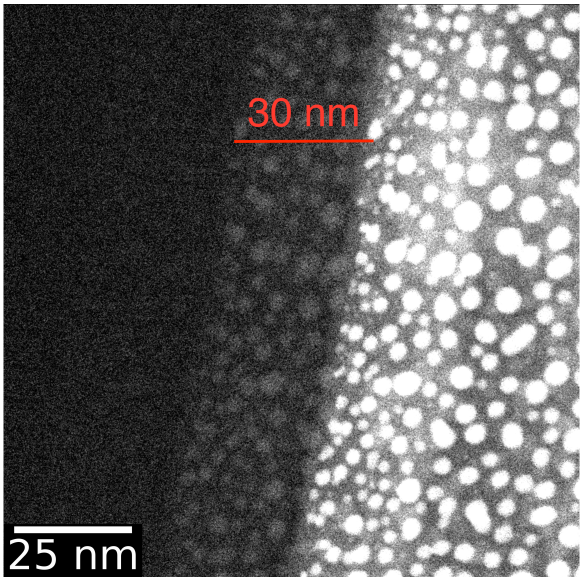

(b)

FIGURE 3. (a) A CCD acquisition of the diffracted probes at the specimen plane with the microscope configured in STEM mode. The asymmetry of the probes' shape is due to aberrations in the projection lenses. An inset of the 0-, +1 and +2 order diffraction probes with a 1D summed profile for comparison of probe intensities. These images are normalized log profiles of the probe. (b) Overlapping STEM images of a test phase object (C membrane with Au nanoparticles for alignment purposes) using multiple diffracted probes. The image is formed by scanning the diffracted probes across the phase object while measuring the amount of scattered electrons using a high angle annular dark field (HAADF) detector. Each of the diffracted probes creates an HAADF image. From these images, we measure the spatial separation by measuring the distance between the bright 0th order image and the lower contrast 1st order image (constructed from the interaction of the 1st order diffraction probe and the phase object). These images were acquired using conventional probe-forming lens settings (convergence angle 6 mrad), and shows a separation of 30 nm between beams.

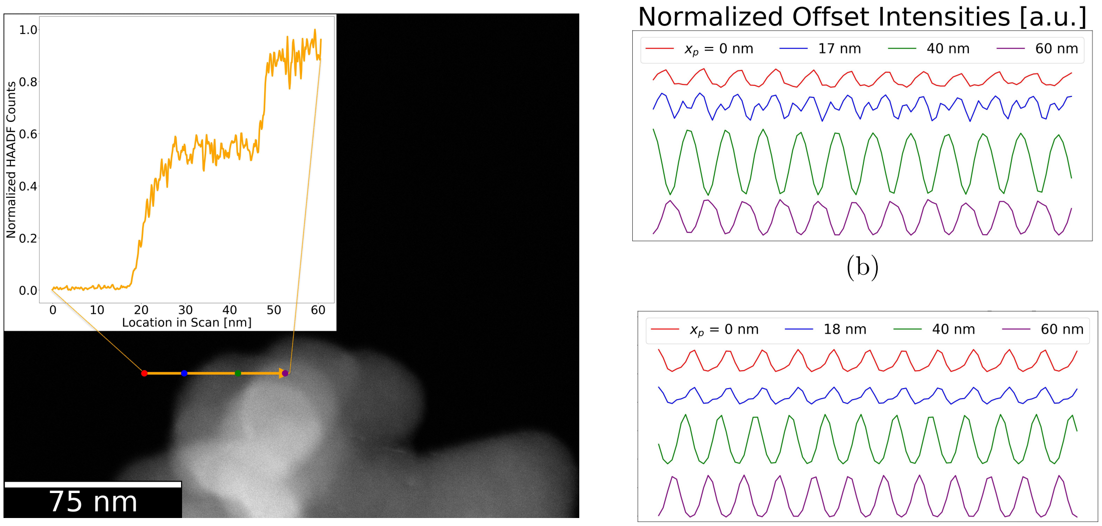

(a)

(b)

(c)

FIGURE 4. (a) A conventional STEM-HAADF image of the graphitic carbon. A line is drawn to mark the position of the +1-order probe as it scanned across the edge of the carbon. The line is in an orientation consistent with the diffraction axis, so that the probes followed one after the other. The inset plot is a smoothed slice of the image along the line scan, or the 1D HAADF profile of the scan. (b) A 1-D slice of the interference fringes (image of the diffraction grating) for various locations along the line scan shown in (a). Note that the fringes translate as the probes scan across the phase object, imparting a different phase value along each location. Note $\mathbf{x_p} = 40$ nm, where the lowest spatial frequency disappears because of destructive interference, leaving fringes with double frequency. (c) Same as (b) but predicted from theory using the HAADF profile as a simulated phase object.The HAADF values were scaled to correspond to a maximum phase shift of 2.3 π rad. with maximum height

Theory

Here we develop a theory to describe the output of a multiple-beam interferometer transmitting through a phase object, which is then scanned. Similar to Cowley's 2-beam electron interferometer proposal [48], we model the wave function of an electron that has been coherently diffracted by a grating into several spots that are focused in the plane of the sample:

$$\psi_0(\mathbf{x}) = \sum_{n=-1}^{+1} s_n\left(\mathbf{x} - n\mathbf{x_0}\right). \tag{2.1}$$

where the complex amplitude unique to the nth diffraction order is described by $s_n(\mathbf{x})$. The spatial separation between diffracted probes can be described by $\mathbf{x_0} = \frac{\lambda f_1}{d}\hat{x}$, where λ is the de Broglie wavelength of the electron, d the spatial frequency of the beam-splitting grating, and f_1 the focal length of the probe-forming lens system.

Usually, a sinusoidal diffraction grating diffracts the electron beam into many diffraction orders. Here, however, we consider a diffraction grating in the aperture plane, fabricated such that all but three of the diffracted spots of varying amplitude c_n are negligible, and they are all sharply peaked with very small beam radii relative to the phase gradient of the phase object transfer function. As such, they can be approximated delta functions:

$$\psi_0(\mathbf{x}) = \sum_{n} c_n \delta\left(\mathbf{x} - n\mathbf{x_0}\right). \tag{2.2}$$

The +1 diffraction spot transmits through an electron-transparent phase object described by a complex transmission function

$$t(\mathbf{x}) = \Theta(-\mathbf{x} + \mathbf{x}_{edge}) + \Theta(\mathbf{x} - \mathbf{x}_{edge})A(\mathbf{x})e^{\imath\phi(\mathbf{x})} \tag{2.3}$$

such that the complex amplitude of the electron wave function immediately after the phase object is

$$\psi_0'(\mathbf{x}) = \psi_0(\mathbf{x})t(\mathbf{x}). \tag{2.4}$$

Note that $1 - |A(\mathbf{x})|^2$ is the probability for an electron to be elastically scattered out of the optical system and $\phi(\mathbf{x})$ is the phase profile of the specimen. For electron-transparent objects, $|A(\mathbf{x})|^2 \approx 1$. The Heavyside theta functions represent the edge of the phase object.

In the experimental setup, the post-specimen optical system of the electron microscope is configured to record a far field diffraction pattern of the sample, which has the effect of spreading and overlapping the separated electron paths to form an interference pattern at the imaging detector (a CCD camera). Thus, this interference pattern can be described by the modulus squared of the Fourier transform of Equation 2.4:

$$I(\mathbf{k}) = |c_0 + c_{-1}e^{2\pi\imath\mathbf{x_0}\cdot\mathbf{k}} + c_{+1}e^{-2\pi\imath\mathbf{x_0}\cdot\mathbf{k}}e^{\imath\phi(\mathbf{x_0})}|^2. \tag{2.5}$$

Fig. 5 shows the behavior of this interference pattern described in Equation 2.5 as a function of the phase ϕ introduced to the +1 diffracted path. Note that the fringes shift laterally for small relative phase shifts as with a 2-path interferometer, but the inclusion of a third path returns a double-spatial-frequency fringe pattern, most noticeable in Fig. 5 when ϕ is an odd multiple of π rad. This can be interpreted as the output of three parallel 2-beam interferometers - one formed by the -1- and +1- order diffracted probes, one by the -1- and 0- order diffracted probes and the

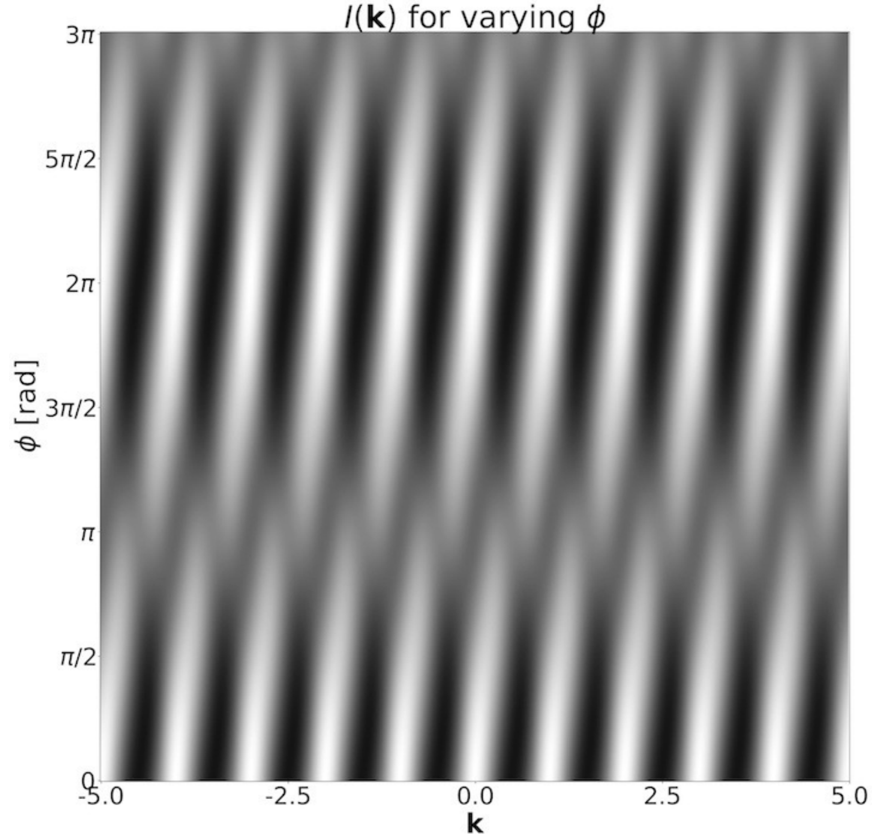

FIGURE 5. Simulated interference profile predicted from Equation 2.5 as a function of the phase ϕ introduced to one path. Here, the horizontal axis is wave number $\mathbf{k}$, the vertical axis is phase ϕ and the color represents $I(\mathbf{k})$. Each row represents a 1D profile of the image of the grating (interference fringes).

other formed by the 0- and +1-order probes. As the phase increases, the 0/+1 and -1/+1 interference fringes translate to the right, while the -1/0 interference fringes stay stationary. The -1/+1 interference between the diffracted probes contributes the double frequency structure seen in Figure 5. Of course, there also exists interference between the higher order diffraction probes, but the intensity of such beams is so low so as to contribute little to the overall interference pattern; i.e., for a typical grating used for these experiments, $|c_{+2}||c_{\pm1}| \ll |c_0||c_{\pm1}|$. This is illustrated in Fig. 3a. The higher order probe interference effects are seen more in the higher frequency fringes structure seen in Fig. 6.

This interferometer can be applied to image phase objects to realize the STEM holography proposed by Cowley [22, 48]. Eq. 2.5 can be expanded to model the behavior of the interference pattern resulting from a nonuniform object that induces a position-dependent phase $\phi(\mathbf{x_p})$ onto electrons. In principle, the object can be scanned in the vicinity of the +1 diffracted probe, but in practice TEM optics can be used to scan the diffraction probes in the sample plane and de-scan the interference pattern. For non-magnetic materials, the position-dependent phase imparted onto an electron by a phase object is given by

$$\phi(\mathbf{x_p}) = C_E \int V(\mathbf{x_p})\; dz, \tag{2.6}$$

where C_E is a constant that is determined by the kinetic energy of the incident electron and $V(\mathbf{x_p})$ is the electric potential of the sample at scan position $\mathbf{x_p}$ [50]; at low resolution and for amorphous materials, we can consider only the mean inner potential. Specimens with a uniform mean inner potential V_0 can be described by a more simplified transmission function,

$$\phi(\mathbf{x_p}) = C_E\; V_0\; T(\mathbf{x_p}), \tag{2.7}$$

where $T(\mathbf{x_p})$ is the thickness of the phase object [50].

Results

We collected interference fringes for a 60 nm line scan with a 1 nm step size. We report fringe contrast of up to 39.7% ± 1.4. We include the image and a 1D profile of the mean along the vertical fringes from which this value was calculated. The fringes from the experiment are summarized in the visualization in Fig. 6a. In this plot, each row corresponds to a mean 1D plot of the interference fringes detected at a single position in the line scan. We compared this to simulated interference fringes from the HAADF profile (Fig. 4a) in Fig. 6a and found the experimental fringe shifts to be consistent with a phase shift of up to 2.3π rad.

Illumination of the phase object with the 0- order diffraction probe

In practice, a scan could be performed where one allows the 0-order diffraction probe to follow the +1-order probe onto the phase object. Mathematically, this would be represented by an $e^{\imath\phi(\mathbf{x})}$ factor in the c_0 term of Equation 2.5. The phase retrieved from the previous scan positions could in principle be utilized to subtract the phase imparted onto the 0-order probe. This analysis is integrated along with our coefficients into the interference pattern shown in Fig. 6b, and we provide the full equation (including the +2 order diffraction probe interaction term) in the supplemental materials.

Recalling Equation 2.7, an electron probe wave function experiences a phase modulation that is directly proportional to the thickness of the phase object $T(\mathbf{x})$. Therefore, a wide variety of TEM samples can be probed using this experimental setup. Additionally, an electron probe experiences a similar phase shift due to local magnetization of specimens, and so this experiment can be expanded to provide nano-magnetic field profiles of magnetic samples, while also providing a path separated interferometric method to explore the Aharonov-Bohm effect.

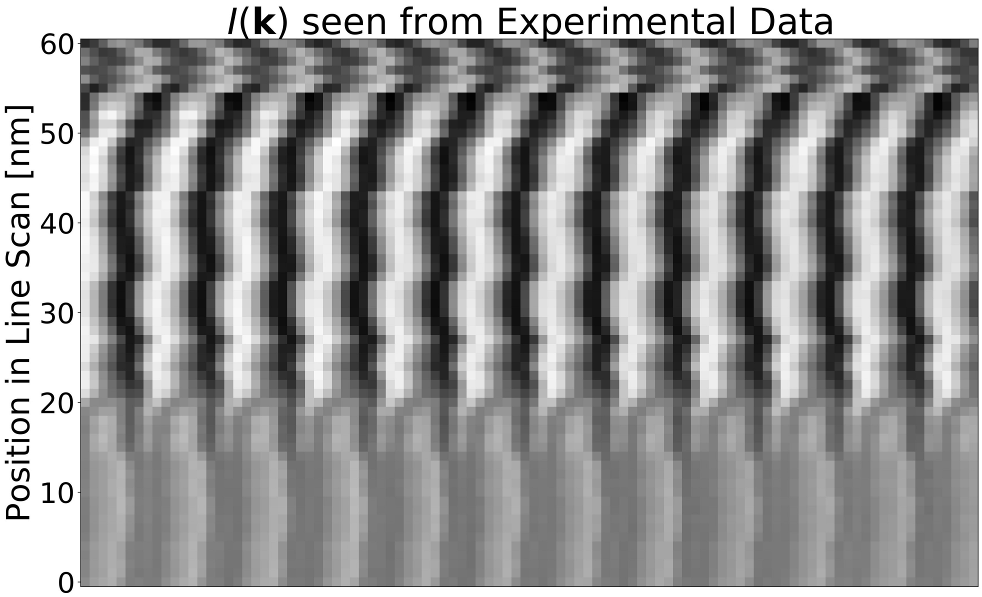

(a)

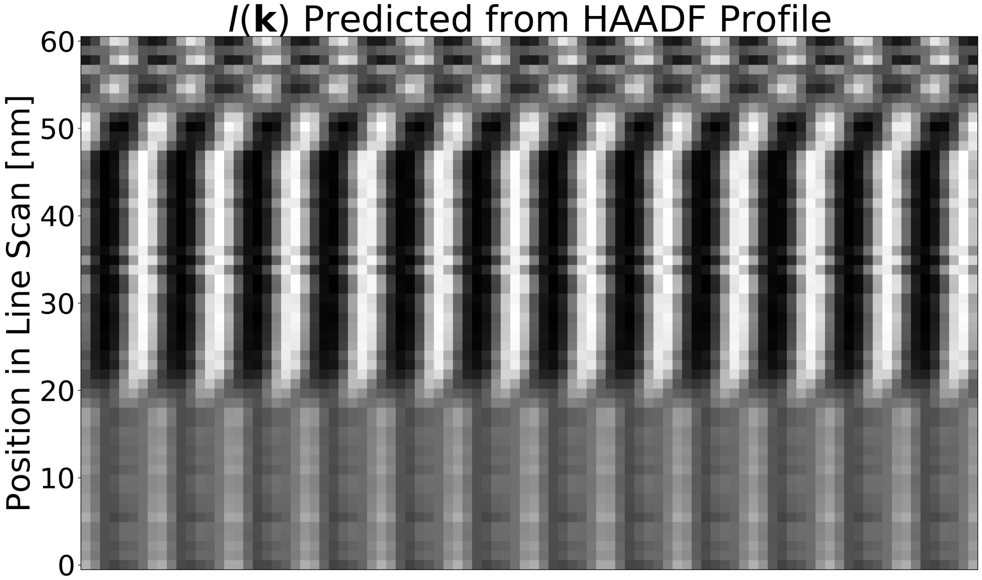

(b)

FIGURE 6. (a) Measured interference fringes using STEM Holography. Along the y-axis are 1D interference fringes, with each line corresponding to the mean pattern at that location in the line scan. Line 0 corresponds to $\mathbf{x}_p = 0$ nm, etc. The change in contrast around position 15 nm is due to the +1-order diffraction probe initiating illumination of the phase object. (b) Predicted interference fringes from the HAADF profile in Fig. 4a. The HAADF values were scaled to correspond to a maximum phase shift of 2.3π rad. Note the agreement with the measured fringes in (a), as well as the blurred fringes over small length scales, due to noise in the HAADF profile.

Conclusion

We have demonstrated a path-separated electron interferometer using a single grating within a widely available, commercial TEM. The nanofabricated phase grating sits within a conventional aperture. We attained spatial separation between electron probes of up to 30 nm, and an interference fringe contrast of up to $39.7 \pm 1.4\%$. We developed a theoretical model of the interference pattern due to three separate paths under the influence of a phase induced to just one path. We performed an experiment in which the interferometer was scanned across a phase object. An independently measured thickness of the test phase object was used as an input to our model, and closely matches the experimental interference pattern.

Our use of a single grating in a modified, user-replaceable condenser aperture in a TEM instrument opens a path to STEM Holography, in which the interferometer is scanned across an electron-transparent phase object in a TEM to form an image of the induced phase. To this end, we are working to invert our theoretical model to quantitatively measure an unknown phase from an experimental scan of the interferometer. STEM Holography has the potential to probe both electrostatic potentials of phase specimens and magnetic fields at sub-nanometer scales. As a path-separated, charged particle-wave interferometer, future work may also include an exploration of the coherence length of electron wavepackets. To be certain, the progress in nano-fabrication techniques for diffraction gratings as well as their easy installation in conventional aperture holders has enabled the use of the electron microscope as an electron optics bench.

Treatment of the second order diffraction probes

One might ask what the second order diffraction probe contribution to the interference pattern is in this multi-armed interferometer. Beginning from Equation (5), we can add the second order terms, while also including the specimen interaction term for the 0-, +1, and +2 terms, since they all illuminate the specimen at some point in the scan. Here, as in Equation 2.5, we only consider one point in the line scan, and so we drop our scan variable $\mathbf{x}_p$. We also choose our origin to be located at the 0-order diffraction probe position.

$$I(\mathbf{k}) = |c_0 e^{\imath\phi(0)} + c_{-1} e^{2\pi\imath \mathbf{x_0}\cdot\mathbf{k}} + c_{+1} e^{-2\pi\imath \mathbf{x_0}\cdot\mathbf{k}} e^{\imath\phi(\mathbf{x_0})} + c_{-2} e^{4\pi\imath \mathbf{x_0}\cdot\mathbf{k}} + c_{+2} e^{-4\pi\imath \mathbf{x_0}\cdot\mathbf{k}} e^{\imath\phi(2\mathbf{x_0})}|^2. \tag{2.8}$$

Expanding this produces a sum of periodic functions. Here we will only keep the first and second frequency terms that include a phase modulation due to the specimen. We'll also consider the probe coefficients to have both amplitude and phase, $c_n = |c_n| e^{\imath\theta_n}$

$$\begin{aligned} I(\mathbf{k}) = \sum_{n=-2}^{+2} |c_n|^2 &+ 2|c_{-2}||c_0| \cos\left(4\pi\mathbf{k}\cdot\mathbf{x}_0 - \phi(0) + \theta_{-2} - \theta_0\right) + 2|c_{-1}||c_0| \cos\left(2\pi\mathbf{k}\cdot\mathbf{x}_0 - \phi(0) + \theta_{-1} - \theta_0\right) \\ &2|c_{-1}||c_{+1}| \cos\left(4\pi\mathbf{k}\cdot\mathbf{x}_0 - \phi\left(\mathbf{x}_0\right) + \theta_{-1} - \theta_{+1}\right) + \\ &2|c_0||c_{+1}| \cos\left(2\pi\mathbf{k}\cdot\mathbf{x}_0 + \phi(0) - \phi\left(\mathbf{x}_0\right) + \theta_0 - \theta_{+1}\right) + \\ &2|c_0||c_{+2}| \cos\left(4\pi\mathbf{k}\cdot\mathbf{x}_0 + \phi(0) - \phi\left(2\mathbf{x}_0\right) + \theta_0 - \theta_{+2}\right) + \\ &2|c_{+1}||c_{+2}| \cos\left(2\pi\mathbf{k}\cdot\mathbf{x}_0 + \phi(\mathbf{x}_0) - \phi\left(2\mathbf{x}_0\right) + \theta_{+1} - \theta_{+2}\right) \end{aligned} \tag{2.9}$$

Supplemental Figure

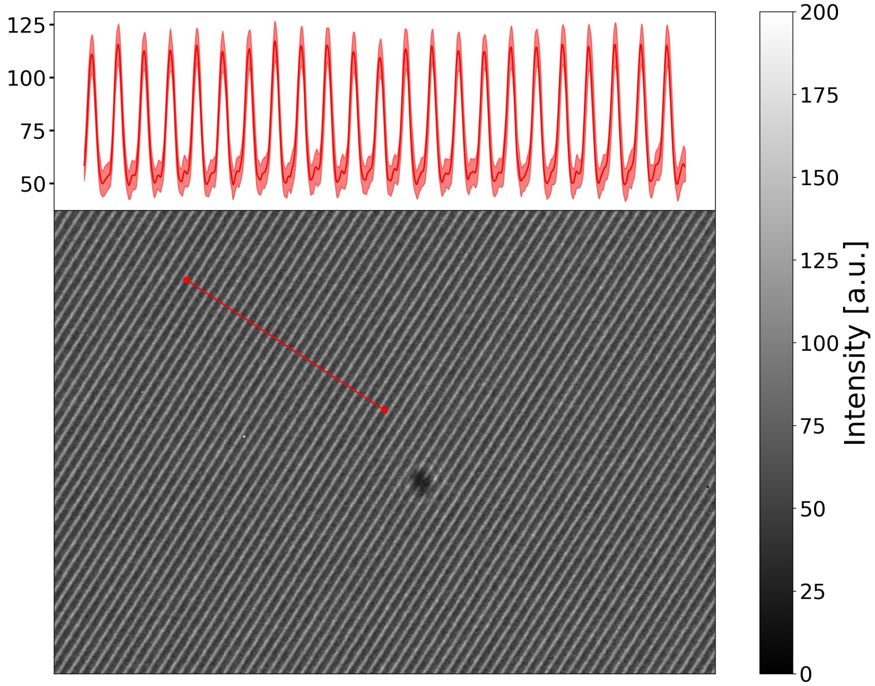

FIGURE 7. Image of interference fringes used to calculate the fringe visibility. Inset shows the 1D average of 100 images along the fringes 'vertical' axis. The color fill represents one standard deviation from the mean for each point. The electron microscope was configured in STEM mode with a spot size of 8 and a convergence angle of 6 mrad.

Chapter Conclusion

In this chapter we presented a path-separated electron interferometer using an amplitude-dividing grating beamsplitter placed in the condenser lens system within a commercial FEI Titan 80-300 TEM. We demonstrated that interference fringes could be recorded and a shift in the fringes could be detected when introducing a phase onto one of the interferometer's arms. We developed a theoretical model of the interference pattern produced by three separate electron beam paths with a phase imparted onto one of the paths. We performed an experiment in which we scanned the focused probe beams from vacuum onto a weak phase object, here thin graphitic carbon, so that only one of the beams would illuminate it. Using an independent measurement of the sample's thickness as an input to our theoretical model, we found that the shift in the simulated interference fringe pattern closely matches our experimental data. Finally, we discussed how such an interferometer may have quantitative imaging applications, and suggested a path forward to STEMH.

CHAPTER III

APPLICATION

Note on ‘Probing Light Atoms at Subnanometer Resolution: Realization of Scanning Transmission Electron Microscope Holography’

Reprinted (adapted) with permission from Fehmi S Yasin *et al.* *Nano Letters* **18**, (11) 7118-23 (2018). Copyright 2018 American Chemical Society.

Benjamin McMorran, Tyler Harvey and I conceived of the experimental setup. Peter Ercius and Colin Ophus provided the specimen. Jordan Pierce fabricated the diffraction grating beamsplitter. Peter Ercius trained me on the microscope, and explained how to use the Gatan K2 Summit camera software. Colin and Peter helped explain how the data structure was saved and provided working examples for how to open and read .dm4 files 300 GB. Jordan Chess provided long hours helping me with code development and optimization. Tyler and I developed theories for STEMH using a weak phase approximation, and then Tyler wrote a general theory of STEMH, resulting in this manuscripts ‘sister’ article, [51]. Colin Ophus contributed a new phase reconstruction idea which Tyler integrated into his theory and I integrated into the final software. Jordan Pierce generated one figure. I recorded all data, generated all but one of the figures, and wrote the supplemental material manuscript with input from coauthors.

Introduction to Probing Light Atoms at Subnanometer Resolution: Realization of Scanning Transmission Electron Microscope Holography

Phase contrast for low-atomic-number, beam-sensitive materials has long been pursued in electron microscopy, seeing the advent of multiple transmission electron microscopy (TEM) and scanning TEM (STEM) techniques over the past 60+ years, including electron holography or interferometry using both wavefront-dividing beamsplitters [4, 9, 23, 31, 32, 33, 52] and amplitude-dividing beamsplitters [5, 34, 35, 36, 38, 39, 53], ptychography [54, 55, 56, 57, 58], cryo-electron microscopy [58, 59, 60], matched illumination and detector interferometry [57, 61], differential phase contrast [62, 63], and more. These techniques have benefited from the development of technologies such as fast readout detectors and aberration correctors that have driven imaging resolution of STEM below 0.41 Å[64] and TEM below 0.43 Å[65].

Several decades ago, an interferometric technique called STEM holography (STEMH) was initially developed as a phase contrast electron imaging technique [16, 17, 18, 19]. These arrangements used a charged biprism wire to split an electron beam into two probes focused at the specimen. With one beam transmitted through the specimen, the interference between the two was recorded. Due to the slow throughput and limited geometries of detectors at the time, STEMH was never widely implemented. The recent advent of fast-readout direct electron detectors enables STEMH as a practical imaging technique. Additionally, advances in FIB fabrication technologies allowed us to expand on this technique with the addition of a static, nanofabricated, amplitude-dividing diffraction grating for use as probe-forming aperture and beam splitter in a multiple-path-separated interferometer [53]. In this article, we provide such a demonstration.

Amplitude-dividing beamsplitters in the form of nanofabricated electron diffraction gratings have been developed by multiple groups. In contrast to wavefront-dividing beamsplitters such as electrostatic biprisms, these diffraction gratings lower the coherence width requirements of the beam, while also allowing for careful shaping of the electron wave fronts phase and amplitude structure [20, 21, 45, 46, 47]. They form symmetric profile probes at the specimen plane (grating's diffraction plane) that are absent of any unwanted edge-diffraction artifacts, and have one passive working part equal in size and shape to conventional apertures, making them easily installable into commercial electron microscopes. Additionally, although many diffraction order probes are generated from the grating, the diffraction efficiency of the grating can be tuned to decrease the intensity in the higher orders [21, 53].

Another technological advance that enables STEMH is the advent of fast-readout direct electron detectors. These detectors are capable of acquiring thousands of images in seconds and are sensitive to individual electrons. Such a fast readout is necessary for any high resolution 4D-STEM imaging technique. In addition to a fast readout of 10^2 fps, the high detective quantum efficiency of such detectors should allow for a decrease in the electron dose seen by the specimen by at least two orders of magnitude [66]. STEMH combines the aforementioned direct electron detector, amplitude-division diffraction gratings, interference fringe phase reconstruction, and aberration correction to provide quantitative phase contrast, including the dc-component with respect to vacuum.

In this article, we provide the theoretical framework for a three-beam, path-separated electron interferometer with a phase imparted onto one or more paths. We then provide two proof-of-principle STEMH images of Au on C, with high-angle annular dark field (HAADF) images for comparison. In HAADF STEM, the beam current is focused to a sub-nanometer width and is scanned across a field of view, dwelling at each location until a sufficient number of high-angle scattering events have illuminated an annulus detector, forming contrast. In STEMH, we extract the phase contrast in these images from the interference fringe patterns using the aformentioned model. STEMH reveals a string-like phase structure in the amorphous carbon region, which is consistent with the thick-bonding theoretical model proposed by Ricolleau et al. [67].

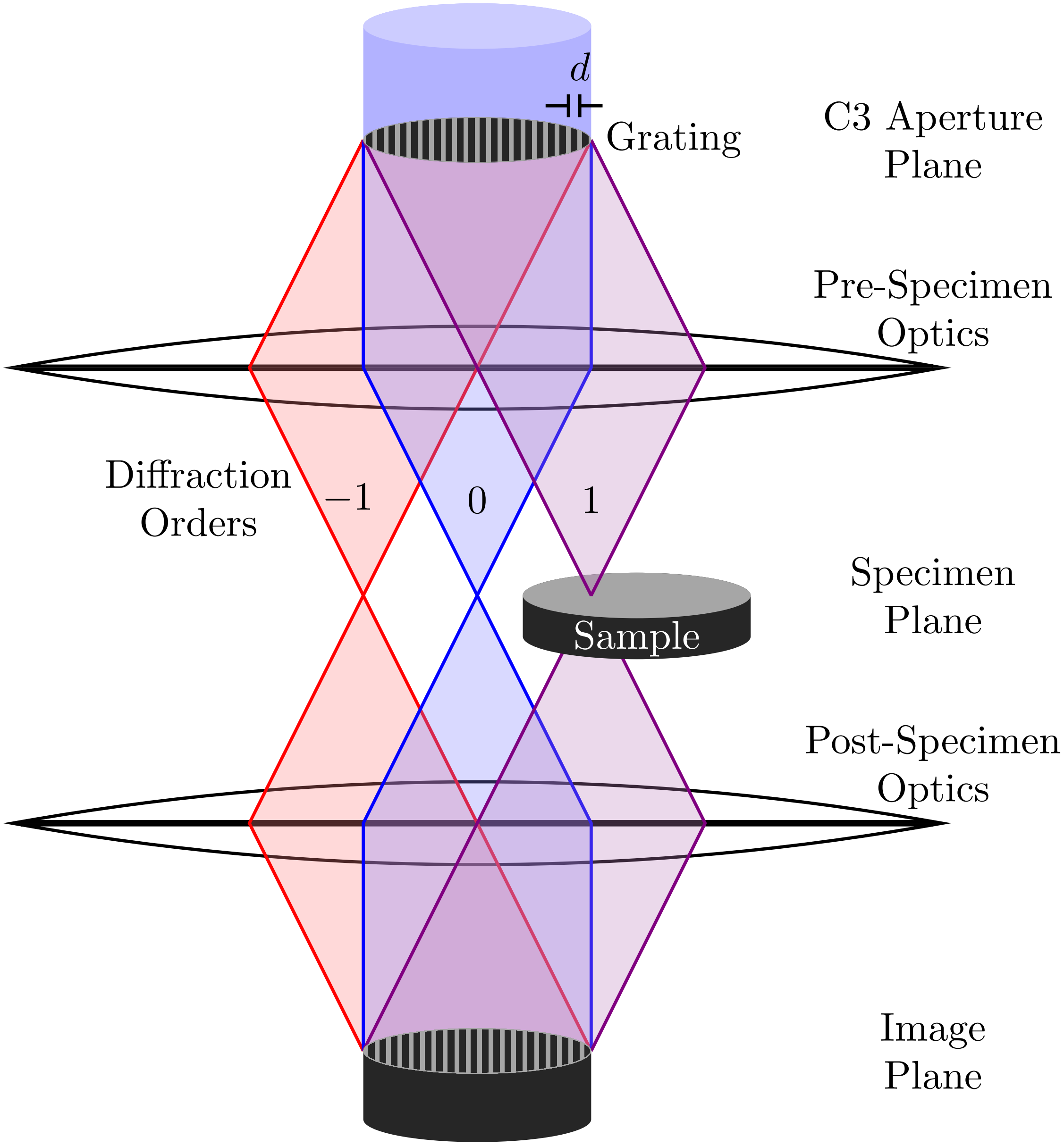

FIGURE 8. STEM holography electron optical setup.

Experimental Setup

As illustrated in Figure 8, the input plane wave electron beam travels down the microscope column to the probe-forming aperture, where a diffraction grating coherently splits the electron beam into multiple diffraction orders that are sharply peaked at the specimen plane, with tens of nanometers spatial separation. The specimen is positioned such that all three diffraction probes, which we'll call $probe_{+1}$, $probe_0$, and $probe_{-1}$ in the text, initially pass through vacuum. These probes are then rastered across the field of view along the same line as the diffraction pattern's orientation using the scanning (deflection) coils in the microscope. $probe_{+1}$ interacts with the specimen while $probe_0$ and $probe_{-1}$ pass through vacuum, acting as reference beams in three parallel interferometers. An interference pattern is focused onto the detector, and the fringes shift as the phase imparted onto the interacting probe varies. Note that as long as the path separation and scan step size are well known, the diffraction probes may be scanned further into the specimen, such that the reference beam also acquires a phase shift. In principle, this reference phase shift, having already been determined at the previous data points in the scan, can be subtracted through post-processing.

As shown in Figure 9a, it is hard to make out interference fringes from a single frame exposed to a beam current of 0.041 nA. Increasing the detector's exposure time to acquire a greater number of events results in fringes discernible to the human eye, as in Figures 9b-9d and 10. Using a computer, however, we can resolve the fringes in a single frame via a Fourier Transform, and so direct electron detectors have decreased STEM convergent beam electron diffraction (CBED) recording time, therefore decreasing the electron dose seen by the specimen.

We inserted a selected area aperture in an image plane of the diffraction probes in order to reduce noise due to unwanted high-angle scattering. This large aperture only blocks high order diffraction probes ($> 4^{th}$ order) which are assumed to be negligible. The passed probes are then recombined through the post specimen optics and interfere in the image plane on the detector. The phase information of each location on the specimen is extracted by a post process described in the Theory and Reconstruction section below.

We performed this experiment on TEAM I, an FEI Titan 80-300 operated at 300 KeV in STEM mode with both probe and image aberration correction and a semi-angle of 30 mrad. A 50 um diameter, 200 nm pitch sinusoidal phase grating is positioned in the Condenser 3 aperture plane. We imaged a specimen consisting of Au nanoparticles on a thin, amorphous carbon support. The images shown in Figures 11b and 11f are reconstructed from a 128 x 296 and 115 x 300 2D scan of 1920 x 1792 images, forming two 4D data sets with a field of view of 11.1 nm x 25.8 nm and 8.6 nm x 22.5 nm, respectively.

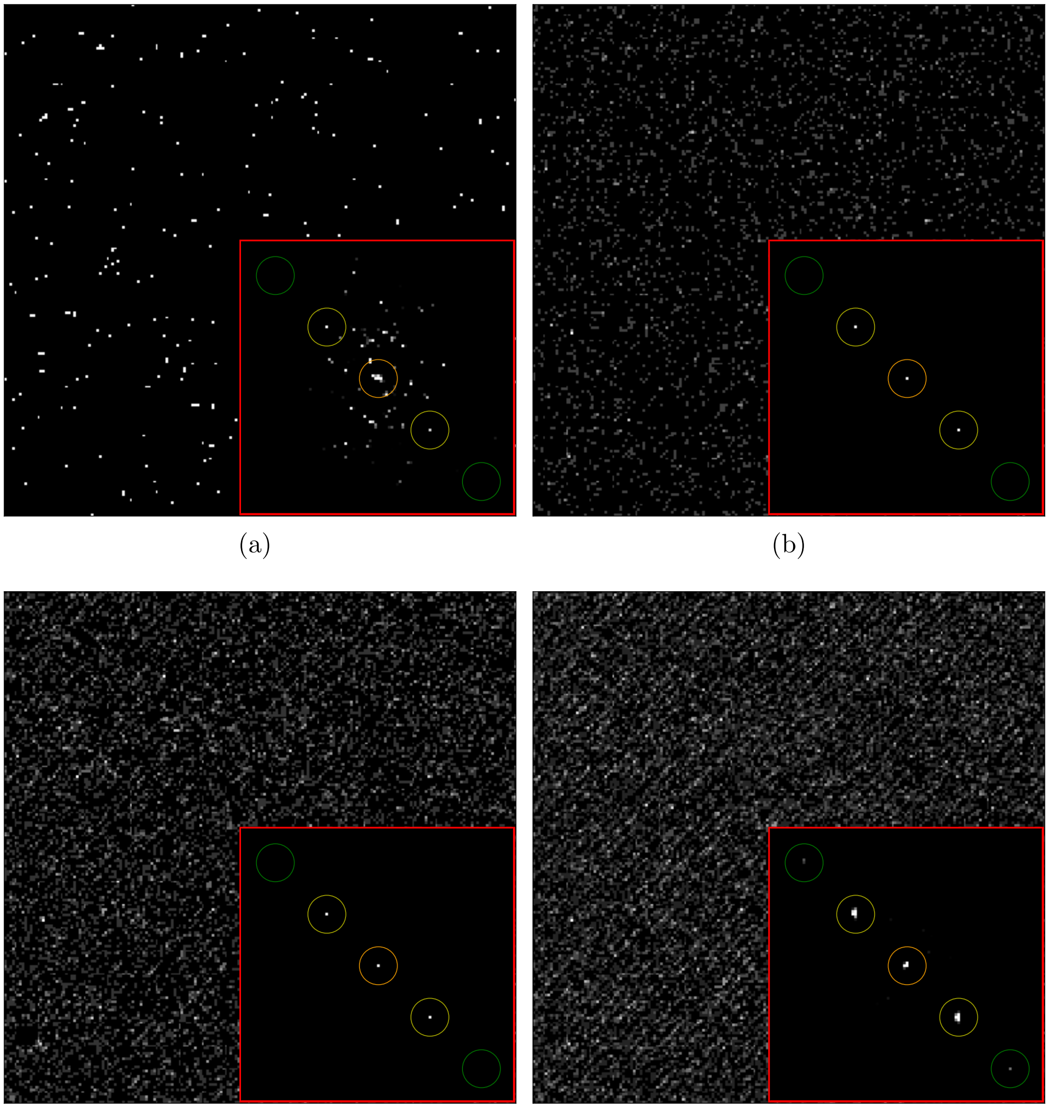

(a) (b)

(c) (d)

FIGURE 9. (a-d) Build-up of single electron events resulting in interference fringes after (a) 0.0025 s, (b) 0.045 s, (c) 0.1425 s, and (d) 0.2875 s. The FFT of each frame is shown in the inset image. Note that frames with 0.0025 s exposure were used to reconstruct the phase image shown in Figure 11.

Theory and Reconstruction

The pre-specimen probe wavefunction is defined to be

$$\psi_i(\mathbf{x}) = a(\mathbf{x} - \mathbf{x}_p) \qquad = \sum c_n a_n \left(\mathbf{x} - \mathbf{x}_p - n\mathbf{x}_0\right) \tag{3.1}$$

where $\mathbf{x}_p$ is the offset-position of our probe, a_n is the phase and intensity distribution of the n^{th} diffraction order, c_n is the complex amplitude of the n^{th} diffraction order probe, and $\mathbf{x}_0$ is the real-space path separation of any one diffraction order probe from it's nearest neighbor. Note that the grating could, in principle, incorporate holographic designs [21] that produce different phase and intensity distributions in each diffraction order, such as vortex beams [20] or aberration-corrected beams [68, 69]. In these experiments, we used a large, straight grating within the aperture, encoding flat phase structure in the probes such that each term in $a(\mathbf{x}-\mathbf{x}_p)$ describes a sharply-peaked, symmetric function that only differs by a linear phase, or $a_n = a_0$.

Recall that the probes are scanning through space at the specimen plane, which is why an offset-position of the probe is needed here. We'll use a specimen transfer function $t(\mathbf{x})$ resulting in a post-specimen wavefunction

$$\psi_f(\mathbf{x}) = a(\mathbf{x} - \mathbf{x}_p) \cdot t(\mathbf{x}), \tag{3.2}$$

where $t(\mathbf{x})$ is the object transmission function. The far field interference pattern at the detector at probe position $\mathbf{x}_p$ is then

$$\begin{aligned} I_p(\mathbf{k}) &= \left|\Psi_f(\mathbf{k})\right|_p^2 \\ &= \left(A_p^*(\mathbf{k}) \otimes T^*(\mathbf{k})\right)\left(A_p(\mathbf{k}) \otimes T(\mathbf{k})\right), \end{aligned} \tag{3.3}$$

where $\otimes$ represents convolution and $*$ represents complex conjugate. We use lower-case and capitilized letters to denote real versus reciprocal space variables, respectively.

Now lets make the assumption that there are only three beams, or $c_{|n|>1} = 0$; $n \in [-1, 0, 1]$, and that only $probe_{+1}$ interacts with the specimen with the other two being reference beams passing through vacuum. Taking the Fourier Transform of 3.3 results in five sharp peaks, which are visible in insets to Figures 9a, 9b, 9c and 9d.

$$\begin{aligned} \mathcal{I}_p(\mathbf{x}) = &\mathcal{I}_{-2}\left(\mathbf{x}_p, \mathbf{x}\right) + \mathcal{I}_{-1}\left(\mathbf{x}_p, \mathbf{x}\right) + \\ \mathcal{I}_0\left(\mathbf{x}_p, \mathbf{x}\right) + &\mathcal{I}_{+1}\left(\mathbf{x}_p, \mathbf{x}\right) + \mathcal{I}_{+2}\left(\mathbf{x}_p, \mathbf{x}\right) \end{aligned} \tag{3.4}$$

Equation 3.4 is expanded into its full form in the supplemental materials. We can extract the specimen's transfer function by integrating around one of the sharp peaks, along the variable $\mathbf{x}$, which would leave us with the transfer function of the scan position variable $\mathbf{x}_p$. We could do this for each peak in $\mathcal{I}_p(\mathbf{x})$, which would give us redundant information for peaks that include a signal from more than one of the interferometers that includes the scanning probe interacting with the specimen. For example, if $probe_{+1}$ is the interaction scanning probe, the object transmission function information probed by the interaction scanning probe is encoded in fringes with spacing $k_0 = \frac{1}{|\mathbf{x}_0|}$ due to interference between the $probe_{+1}$ and $probe_0$. This period corresponds to the -1- and $+1$- order peaks in $\mathcal{I}_p(\mathbf{x})$, from which the transmission function can be extracted.

This information is also encoded in fringes with spacing $k_0 = \frac{1}{2|\mathbf{x}_0|}$ due to interference between $probe_{+1}$ and $probe_{-1}$, and can therefore be extracted from the -2- and $+2$-order peaks in $\mathcal{I}_p(\mathbf{x})$. In summary, for a three beam interferometer in which one first order diffraction probe interacts with the specimen, the object transmission function information is stored in both the the first and second orders, respectively, of the Fourier transform of the interference fringe image.

A non-negligible $+2$-order diffraction probe $probe_{+2}$ complicates this picture, and the -2 and $+2$ peaks in $\mathcal{I}_p(\mathbf{x})$ also contain that information via interference with $probe_0$. Because the nanofabricated gratings are designed such that $c_{n>1}$ should be weak, we assume that it is negligible.

We can also make the assertion that the specimen function in vacuum is just 1, simplifying equation 3.4 even further. Integrating around $\mathcal{I}_{+1}\left(\mathbf{x}_p, \mathbf{x}\right)$ in equation 3.4, using $a_0\left(\mathbf{x}\right)$ as a kernel, and noting that $A_0\left(\mathbf{k}\right)$ is a circular aperture, we arrive at the solution.

$$\begin{aligned}&\int_{\Omega(+\mathbf{x}_0)} a_0\left(\mathbf{x}\right)\mathcal{I}_{+1}\left(\mathbf{x}_p, \mathbf{x}\right) d\mathbf{x}\\ &\qquad = c_0^* c_{+1} h\left(\mathbf{x}_p\right) \otimes t^*\left(\mathbf{x}_0 + \mathbf{x}_p\right)\end{aligned} \tag{3.5}$$

where $h\left(\mathbf{x}_p\right) = |a_0\left(\mathbf{x}_p\right)|^2$. The full derivation is provided in both the supplemental materials and another manuscript that provides a full treatment of the general theory of STEMH [70].

To summarize the numerical object wave reconstruction procedure:

1. At each probe position, take the Fourier transform of the interference fringe pattern, resulting in equation (3.4).
2. Isolate a small (we used $< 10 \times 10$ pix^2) region around a peak that contains the desired object wave information, $\mathcal{I}_{+1}(\mathbf{x}_p, \mathbf{x})$.
3. Define a kernel $a_0(\mathbf{x})$ by taking the Fourier transform of a reference image of the interference fringes, i.e. an image when all three probes pass through vacuum, and isolate a small region around the center peak.
4. Multiply these two peaks and integrate, taking the complex conjugate, equation (3.11).
5. Repeat for each pattern in the scan, i.e. each x_p value.

Phase-thickness relation

The specimen transfer function contains an amplitude and phase, which can be used to calculate the thickness of a specimen. For a non-magnetic specimen, the phase imparted onto an electron wave-front is proportional to the electrostatic potential projected through the bulk of the specimen [53]. For amorphous materials, we may consider only the mean inner potential, V_i. Thus,

$$\phi = C_E V_i T(\mathbf{x}_p), \tag{3.6}$$

where $T(\mathbf{x}_p)$ is the thickness of the specimen for each location in the scan, $\mathbf{x}_p$, $C_E = \frac{2\pi}{\lambda}\frac{e}{E}\frac{E_0+E}{2E_0+E}$, λ is the relativistic wavelength of the electron, 1.97 pm for $E = 300$ keV, where E is the kinetic energy of the electron, E_0 is the rest energy of the electron, and e is the electron unit charge.

Phase uncertainty

The theory of phase detection uncertainty in electron holography has been worked out in detail by Lichte et al. and de Ruijter et al. [71, 72], whose work was experimentally supported by Harscher and Lichte [73]. If we only consider the counting statistics for the number of electrons per unit area of the detector at any time (shot noise), the standard deviation for detection of the phase from interference fringes with visibility $\mathcal{V} = \frac{I_{max}-I_{min}}{I_{max}+I_{min}}$ is

$$\sigma_{\phi_{th}} = \sqrt{\frac{2}{\mathcal{V}^2 N}}, \tag{3.7}$$

where N is the number of electrons in the measurement area.

Detectors will also contribute to the phase uncertainty, and their contribution is typically characterized by a detective quantum efficiency,

$$DQE = \frac{(SNR)^2_{out}(u)}{(SNR)^2_{in}(u)}, \tag{3.8}$$

where $(SNR)_{out}(u)$ and $(SNR)_{in}(u)$ are signal-to-noise ratios at the output and input of the detector as a function of spatial frequency, u [73]. The DQE modifies equation 3.7 to be

$$\sigma_{\phi_{th}} = (DQE)^{-\frac{1}{4}} \sqrt{\frac{2}{\mathcal{V}^2 N}}. \tag{3.9}$$

For our experiment, the number of electrons per frame was estimated by summing the intensity values in a frame to be $N \approx 10^5$ and we measured our fringe visibility

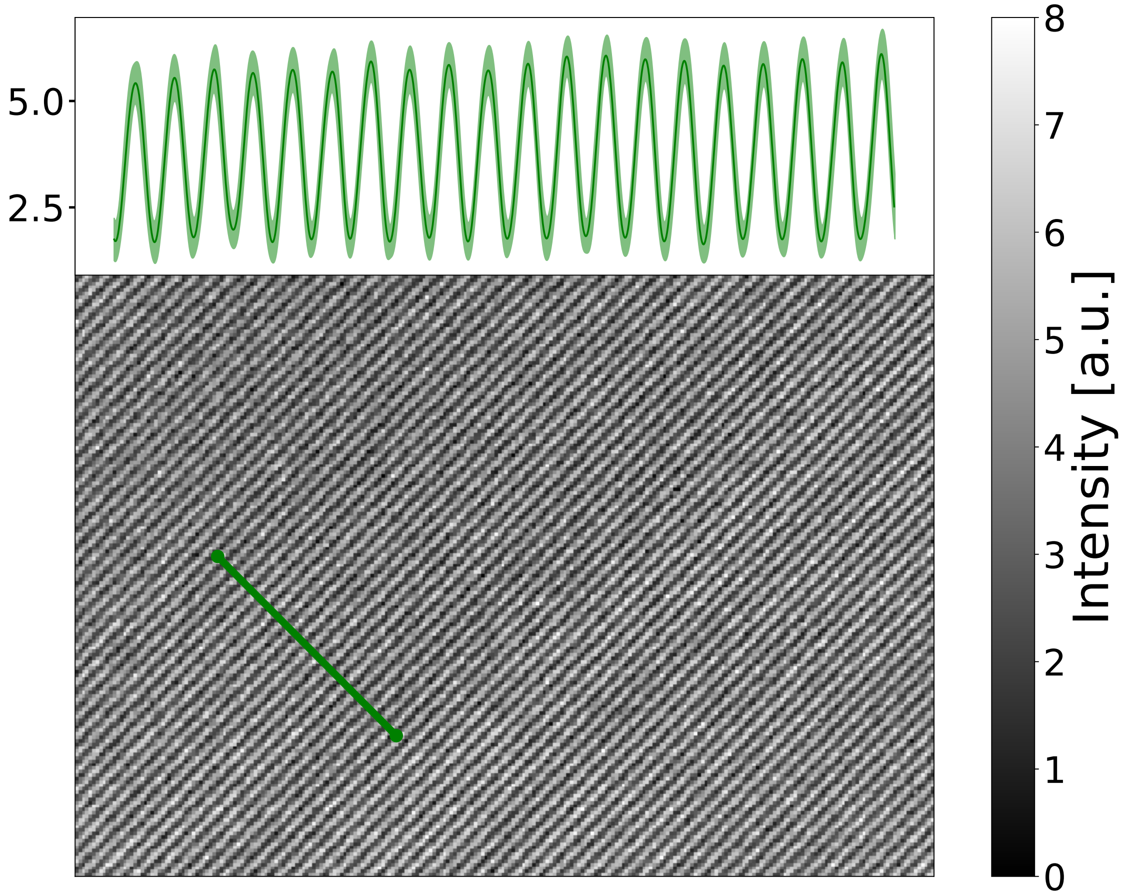

FIGURE 10. Mean interference fringes averaged over the scan with the background subtracted. The inset shows a 1D profile of the sum of fringes along the direction perpendicular to the line trace shown.

from Figure 10 to be $\mathcal{V} = 42.7\% \pm 4.8$. The predicted fringe visibility from an ideal three beam interferometer depends on the phase imparted onto $probe_{+1}$. The fringe spacing at the camera was $\approx 0.38 \times f_N$, where f_N is the Nyquist frequency. At this spatial frequency, the Gatan K2 Summit camera has a $DQE \approx 0.56$ [66]. Using these values, we plot the numerically calculated $\mathcal{V}$ and $\sigma_{\phi_{th}}$ in the supplemental materials. The mean theoretical uncertainty in phase measurement is $\sigma_{\phi_{th}} < 15$ mrad when $probe_{+1}$ transmits through a weak phase object.

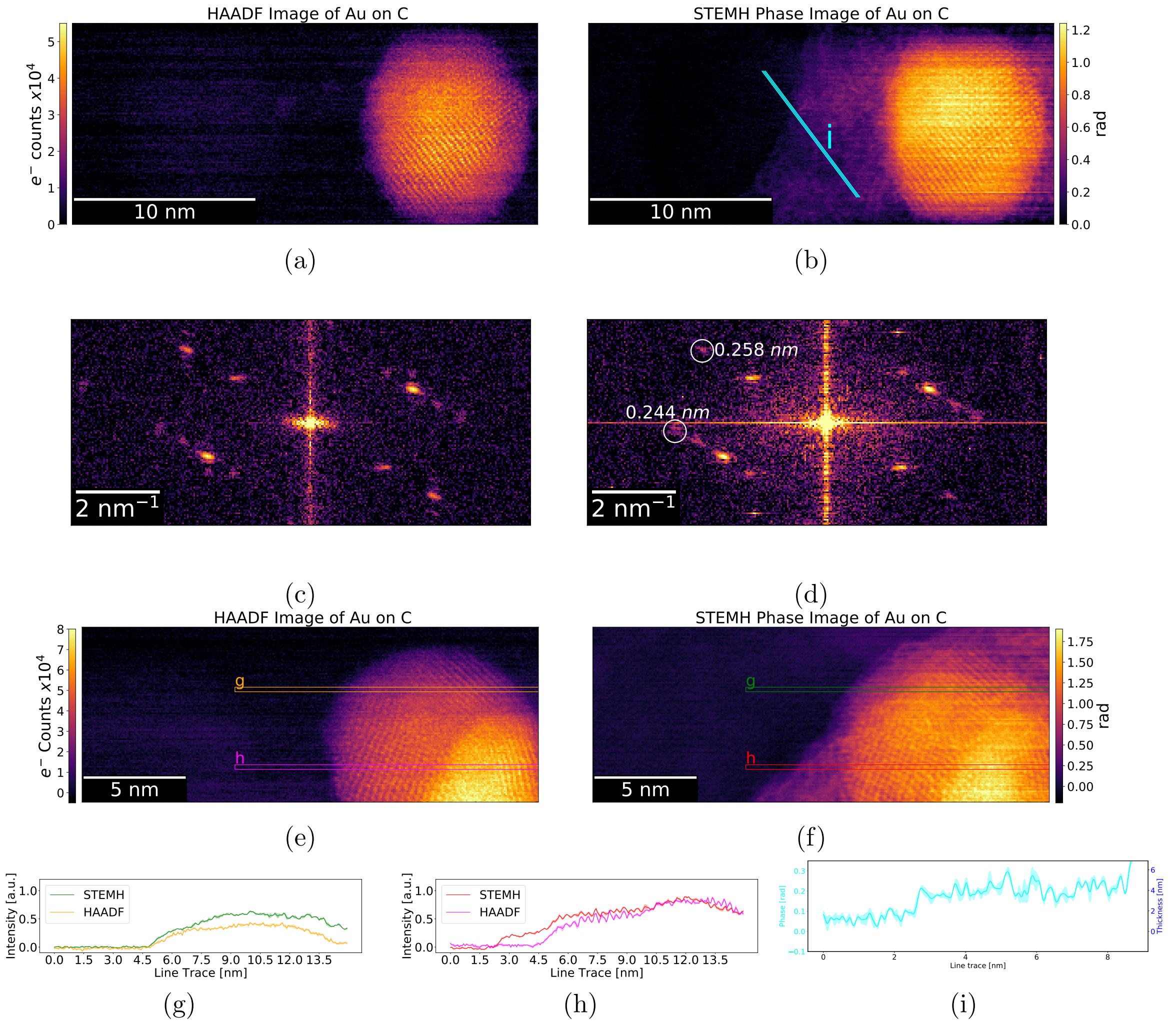

(a) (b) (c) (d) (e) (f) (g) (h) (i)

FIGURE 11. (a,e) Conventional annular dark field images of two different Au nanoparticles on thin C support. (b,f) Phase reconstruction of the same regions using STEMH. (c-d) Corresponding Fourier Transforms of (a) and (b). (g-h) Selected line traces from (e-f), highlighting the low atomic number material contrast seen using STEMH. The profiles are normalized to the maximum value of each image after offsetting to a mean value of zero in vacuum. (i) Selected line trace from (b) along just the carbon substrate, from which the thickness is calculated. (g-i) are plots of the mean along three line traces with the root mean square of the the deviations shaded.

Results and Discussion

STEMH Phase Contrast

The STEMH phase reconstructions and HAADF images of two randomly oriented Au nanoparticles embedded on a thin amorphous carbon film are shown in Figure 11. Compared to the HAADF image, STEMH allows for a much higher contrast of the thin amorphous carbon. Additionally, the dc-component of the phase is reconstructed using STEMH, resulting in a comparable signal with the HAADF, but with additional amorphous carbon signal barely visible in the HAADF. Figure 11d shows that under the experimental conditions we used, STEMH has 0.24 nm resolution of the Au atomic lattice, comparable to the HAADF resolution shown in 11c. Notice how the high frequency information between the two techniques are comparable, whereas the STEMH reconstruction contains much more low frequency information because of the higher contrast on the carbon substrate. Note that these scans were under-sampled in order to achieve a large field of view and decrease both the scan time and file size. The achievable probe size for STEM is sub-angstrom as discussed in the introduction, suggesting that STEMH should be able to achieve even higher resolution than we report.

Figures 11g - 11h shows selected line traces along the carbon film and Au nanoparticles for both the STEMH and HAADF signals. For comparison, the signals are normalized to the maximum value of each image after offsetting to a mean value of zero in vacuum. For 11h the STEMH signal begins to rise earlier than the HAADF due to the amorphous carbon preceding the Au nanoparticles. In 11g, the two signals rise simultaneously because the nanoparticle hangs off of the edge of the carbon. However, the STEMH signal continues to rise around 7 nm, because unlike HAADF STEM the

STEMH signal is sensitive to the carbon film lying beneath the Au nanoparticle. This is due to STEMH's phase contrast, resulting in a gap between the two signals after 7 nm.

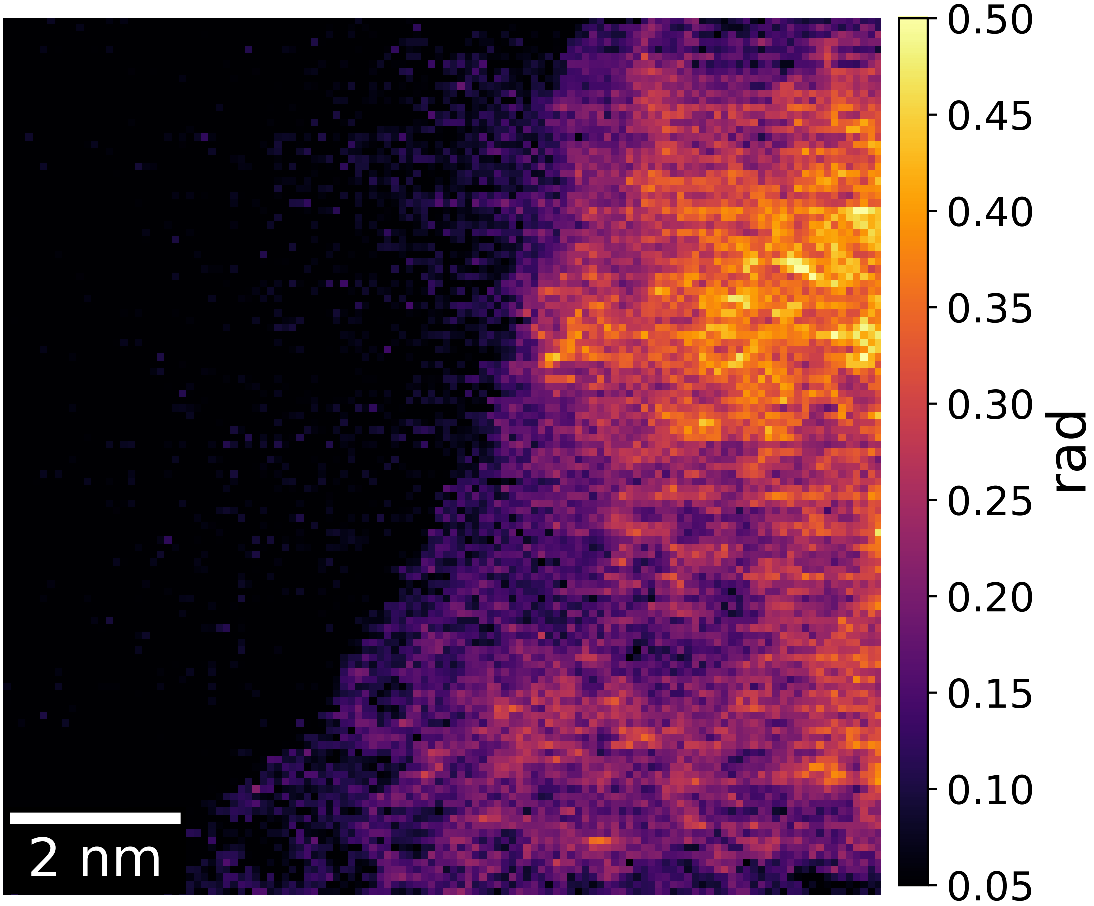

FIGURE 12. Inset from center of Figure 11b in a carbon-only region to enhance contrast.

The line trace in Figure 11b follows a path along the amorphous carbon film and is plotted in Figure 11i. The thickness calculated from equation (3.6) is shown on the right vertical axis. Interestingly, the carbon in Figures 11b and 11f, isolated in Figure 12, shows a string-like topography, which is consistent with a thick-bonding model detailed by Ricolleau, et al. in 2013 [67].

We previously assumed that $probe_{+2}$ was weak, or $c_{+2} < \frac{c_{+1}}{10}$. This results in a phase signal $< \frac{1}{10}$ the $probe_{+1}$ signal. Such a weak signal is present in Figures 11b and 11f in the form of a 'shadow' image of the nanoparticle in vacuum, although it is weak enough to be barely identifiable above the noise from the primary signal on carbon.

As shown in the previous section, however, this signal is on the same order or larger than our theoretical uncertainty, which is confirmed by our measurement of uncertainty in the phase. Here, we measured the deviation from the mean for both a single line and an area of 50 lines within the vacuum region of Figure 11b. We found that for a single line, $\sigma_{\phi_{exp}} = 30$ mrad and $\sigma_{\phi_{exp}} = 35$ mrad for an area of 50 lines. This difference can be attributed to scan noise. The increase in noise between theory and experiment is consistent with contributions due to higher order probes, and so future consideration should be taken when designing gratings so as to optimize the output SNR. Alternatively, a smaller selected area aperture could be used to block higher orders.

Conclusions

In this article, we demonstrated sub-nanometer resolution electron phase imaging using STEMH, a multiple-arm, path-separated interferometer with a phase imparted onto one or more paths. We measured a fringe visibility of $\mathcal{V} = 42.7\%$ experimental uncertainty in phase measurement to be $\sigma_{\phi_{exp}} \approx 0.03$ rad. We then provided two 0.24 nm resolution phase-contrast images of Au nanoparticles on a thin carbon substrate, with conventional HAADF images for comparison.

STEMH provides quantitative phase contrast, including the dc-component, which we utilized to analyze the thickness of the carbon support. In addition to thickness mapping due to the electrostatic potential within nanomaterials, STEMH enables magnetic field mapping at subnanometer resolution. With an aperture inserted to block higher order probes, the electron scanning coils can be utilized to image electric and magnetic fields surrounding a material without illuminating the material at all. Recall that we used a straight grating in this experiment to prepare sharply-peaked, symmetric probes at the sample plane. Note, however, that different phase-structured diffraction grating designs can be used to holographically vary the complex amplitude c_n of the diffraction orders [21, 46, 47, 61], potentially enabling more complicated electron-specimen interactions with signals extractable via STEMH. Finally, future additions of faster readout detectors and different grating designs would further reduce the electron dose, potentially allowing STEMH to image beam-sensitive, bio-molecular materials, electronics and magnetic materials at atomic resolution.

Full form of equation 3.4

$$
\begin{aligned}
\mathcal{I}_p(\mathbf{x}) = \sum_{n=-1}^{+1} \left| c_n t\left(n\mathbf{x}_0 + \mathbf{x}_p\right)\right|^2 & \\
+ c_{-1}^* c_0 \left[a_{-1}^*\left(\mathbf{x} + 1\mathbf{x}_0\right) t^*\left(\mathbf{x} + \mathbf{x}_p\right)\right] & \otimes \left[a_0\left(\mathbf{x} + 1\mathbf{x}_0\right) t\left(\mathbf{x} + 1\mathbf{x}_0 - \mathbf{x}_p\right)\right] \\
+ c_0^* c_{-1} \left[a_0^*\left(\mathbf{x} - 1\mathbf{x}_0\right) t^*\left(\mathbf{x} - 1\mathbf{x}_0 + \mathbf{x}_p\right)\right] & \otimes \left[a_{-1}\left(\mathbf{x} - 1\mathbf{x}_0\right) t\left(\mathbf{x} - \mathbf{x}_p\right)\right] \\
+ c_{-1}^* c_{+1} \left[a_{-1}^*\left(\mathbf{x} + 2\mathbf{x}_0\right) t^*\left(\mathbf{x} + 1\mathbf{x}_0 + \mathbf{x}_p\right)\right] & \otimes \left[a_{+1}\left(\mathbf{x} + 2\mathbf{x}_0\right) t\left(\mathbf{x} + 1\mathbf{x}_0 - \mathbf{x}_p\right)\right] \\
+ c_{+1}^* c_{-1} \left[a_{+1}^*\left(\mathbf{x} - 2\mathbf{x}_0\right) t^*\left(\mathbf{x} - 1\mathbf{x}_0 + \mathbf{x}_p\right)\right] & \otimes \left[a_{-1}\left(\mathbf{x} - 2\mathbf{x}_0\right) t\left(\mathbf{x} - 1\mathbf{x}_0 - \mathbf{x}_p\right)\right] \\
+ c_0^* c_{+1} \left[a_0^*\left(\mathbf{x} + 1\mathbf{x}_0\right) t^*\left(\mathbf{x} + 1\mathbf{x}_0 + \mathbf{x}_p\right)\right] & \otimes \left[a_{+1}\left(\mathbf{x} + 1\mathbf{x}_0\right) t\left(\mathbf{x} - \mathbf{x}_p\right)\right] \\
+ c_{+1}^* c_0 \left[a_{+1}^*\left(\mathbf{x} - 1\mathbf{x}_0\right) t^*\left(\mathbf{x} + \mathbf{x}_p\right)\right] & \otimes \left[a_0\left(\mathbf{x} - 1\mathbf{x}_0\right) t\left(\mathbf{x} - 1\mathbf{x}_0 - \mathbf{x}_p\right)\right]
\end{aligned}
\tag{3.10}
$$

Collecting the ℓ^{th} peak terms $a\left(\mathbf{x} + \ell\mathbf{x_0}\right)$, we can write this in the simpler form seen in equation 3.4.

Derivation of transfer function reconstruction

Let us integrate out the $\mathbf{x}$ variable around the +1 order peak in $\mathcal{I}_p(\mathbf{x})$, using a_0 as a kernel.

$$
\int_{\Omega(+\mathbf{x}_0)} a_0\left(\mathbf{x}\right) \mathcal{I}_{+1}\left(\mathbf{x}_p, \mathbf{x}\right) d\mathbf{x} = \int c_0^* c_{+1} a_0\left(\mathbf{x}\right) \left[a_0^*\left(\mathbf{x}\right) t^*\left(\mathbf{x} + 1\mathbf{x}_0 + \mathbf{x}_p\right)\right] \otimes a_{+1}\left(\mathbf{x}\right) \mathrm{d}\mathbf{x}
$$

Using the commutivity of convolutions:

$$
= c_0^* c_{+1} \int \int a_0\left(\mathbf{x}\right) a_{+1}\left(\mathbf{x} - \mathbf{x}'\right) \left[a_0^*\left(\mathbf{x}'\right) t^*\left(\mathbf{x}' + 1\mathbf{x}_0 + \mathbf{x}_p\right)\right] \mathrm{d}\mathbf{x}\mathrm{d}\mathbf{x}'
\tag{3.11}
$$

Because $a_n\left(\mathbf{x}\right)$ is a symmetric function, $\int a_0\left(\mathbf{x}\right)a_{+1}\left(\mathbf{x}-\mathbf{x}'\right)d\mathbf{x} = a_0^*\left(\mathbf{x}'\right)\otimes a_{+1}\left(-\mathbf{x}'\right) = a_0\left(-\mathbf{x}'\right)\otimes a_{+1}\left(\mathbf{x}'\right) = a_0\left(\mathbf{x}'\right)\otimes a_{+1}\left(\mathbf{x}'\right)$. We can simplify this further using the convolution theorem, and noting that the circular aperture $A_0\left(\mathbf{k}\right)$ is a top hat function:

$$A_m\left(\mathbf{k}\right) = A_0\left(\mathbf{k}\right) = \begin{cases} \frac{1}{\pi K^2} & |\mathbf{k}| \leq K \\ 0 & |\mathbf{k}| > K \end{cases} \tag{3.12}$$

$$\begin{aligned}
&\int_{\Omega(+\mathbf{x}_0)} a_0\left(\mathbf{x}\right)\mathcal{I}_{+1}\left(\mathbf{x}_p, \mathbf{x}\right)d\mathbf{x} \\
&\qquad = c_0^* c_{+1}\int\int e^{-2\pi i\mathbf{k}\cdot\mathbf{x}'}A_0\left(\mathbf{k}\right)A_{+1}\left(\mathbf{k}\right)\left[a_0^*\left(\mathbf{x}'\right)t^*\left(\mathbf{x}'+1\mathbf{x}_0+\mathbf{x}_p\right)\right]d\mathbf{k}d\mathbf{x}' \\
&\qquad = c_0^* c_{+1}\int\int e^{-2\pi i\mathbf{k}\cdot\mathbf{x}'}|A_0\left(\mathbf{k}\right)|^2\left[a_0^*\left(\mathbf{x}'\right)t^*\left(\mathbf{x}'+1\mathbf{x}_0+\mathbf{x}_p\right)\right]d\mathbf{k}d\mathbf{x}' \\
&\qquad = c_0^* c_{+1}\int\int e^{-2\pi i\mathbf{k}\cdot\mathbf{x}'}A_0\left(\mathbf{k}\right)\left[a_0^*\left(\mathbf{x}'\right)t^*\left(\mathbf{x}'+1\mathbf{x}_0+\mathbf{x}_p\right)\right]d\mathbf{k}d\mathbf{x}' \\
&\qquad = c_0^* c_{+1}\int a_0\left(\mathbf{x}'\right)\left[a_0^*\left(\mathbf{x}'\right)t^*\left(\mathbf{x}'+1\mathbf{x}_0+\mathbf{x}_p\right)\right]d\mathbf{x}' \\
&\qquad = c_0^* c_{+1}\int |a_0\left(\mathbf{x}'\right)|^2 t^*\left(\mathbf{x}'+1\mathbf{x}_0+\mathbf{x}_p\right)d\mathbf{x}' \\
&\qquad = c_0^* c_{+1}\left(|a_0\left(\mathbf{x}_p\right)|^2\right)^* \star t^*\left(\mathbf{x}_0+\mathbf{x}_p\right) \\
&\qquad = c_0^* c_{+1}|a_0\left(-\mathbf{x}_p\right)|^2 \otimes t^*\left(\mathbf{x}_0+\mathbf{x}_p\right) \\
&\qquad = c_0^* c_{+1}h\left(\mathbf{x}_p\right)\otimes t^*\left(\mathbf{x}_0+\mathbf{x}_p\right)
\end{aligned} \tag{3.13}$$

Since a_0 is symmetric, $h\left(\mathbf{x}_p\right) = |a_0\left(\mathbf{x}_p\right)|^2$. For the case where $a_n\left(\mathbf{x}\right)$ is asymmetric, refer to the supporting information of our other article[70].

Numerical calculation of $\sigma_{\phi_{th}}$

For an ideal three beam interferometer, the three probes are of equal amplitude ($c_n \approx \frac{1}{\sqrt{3}}$). In the following calculation, we simulated a phase grating with the following transmission function:

$$G\left(\mathbf{k}\right) = \exp\left(\Delta\phi \; i \frac{\left(1 + cos\left(\frac{2\pi}{d}\mathbf{k}\right)\right)}{2} \right) \times A_0(\mathbf{k}), \tag{3.14}$$

where $\Delta\phi$ is the phase depth, a complex coefficient that determines the diffraction grating efficiency and wavefunction amplitude loss, while d is the grating pitch. For the simulation, we used $\Delta\phi = 2.869$, which corresponds to diffraction probe amplitudes of $c_n = 0.299$, for $n \in [-1, 0, 1]$. The grating pitch was $d = 160$ nm and the diameter was 50 μm. We then calculated the probe wavefunction and applied a phase to $probe_{+1}$. We calculated the fringe visibility from equation (3.15), which utilizes the fast Fourier transform of the fringe pattern. There are two fringe spacings, and so equation (3.15) calculates the fringe visibility of the m^{th} FFT peak, corresponding to the $probe_{+1}/probe_{-1}$ interferometer ($m = 2$) and the $probe_{+1}/probe_0$ interferometer ($m = 1$).

$$\mathcal{V} = \frac{\mathcal{I}_m + \mathcal{I}_m}{\mathcal{I}_0} = \frac{\Delta I}{2\langle I \rangle} \tag{3.15}$$

As shown in Figure 13a, the fringe visibility $\mathcal{V}$ varies between 0 % and 91 %. This of course means that for a pure phase grating, the phase uncertainty diverges at $\phi = \ell 2\pi$, where ℓ is an integer value. Realistically, these gratings are partially amplitude gratings, and so the visibility is nonzero in vacuum. The corresponding phase uncertainty is shown in Figure 13b. Since the phase information is measured

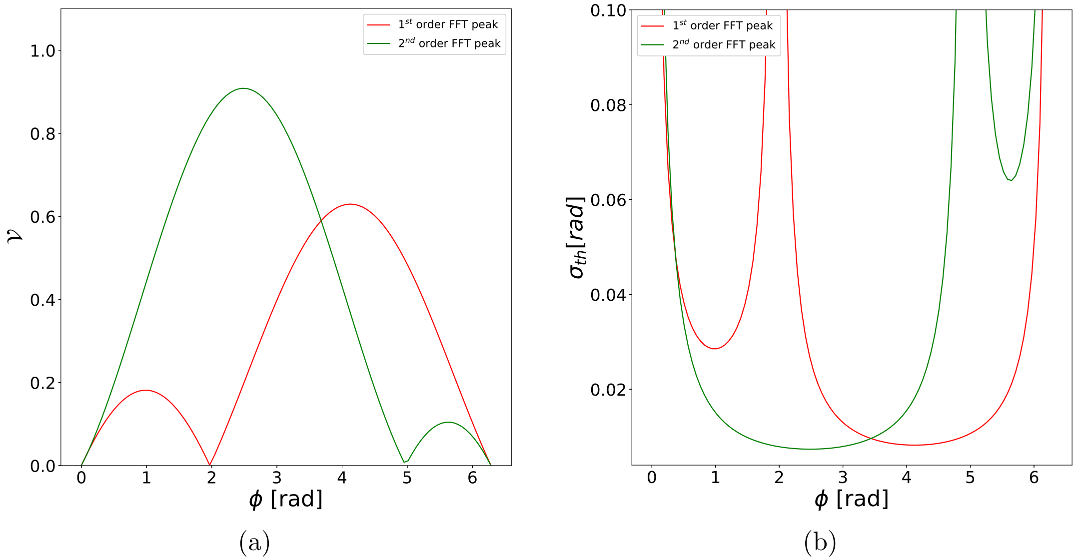

FIGURE 13. (a) The fringe visibility and (b) root-mean-squared uncertainty as a function of phase imparted onto $probe_{+1}$ for both $m = 1$ (red) and $m = 2$ (green).

in both interferometers, STEMH can utilize both signals to decrease the phase uncertainty over a range of phase values.

Chapter Conclusion

In this chapter we demonstrated scanning transmission electron microscope holography at sub-nanometer resolution. We presented a theoretical model to extract the transmission function of a specimen from directly imaging and analyzing the interference patterns at each point in an image scan. We perform the technique to image gold nanoparticles on a thin carbon substrate. In the next chapter, we will present a further innovation to improve the ability of this electron interferometer to probe more fundamental physics, image across large fields of view, and lower the electron dose by increasing the signal to noise ratio of the interference fringe patterns.

CHAPTER IV

MEASUREMENT

Note on ‘A tunable path-separated electron interferometer with an amplitude-dividing grating beamsplitter.’

Reprinted from Fehmi S Yasin *et al.* *Applied Physics Letters* **113**, 233102 (2018), with the permission of AIP Publishing.

Benjamin McMorran and Toshiaki Tanigaki first chatted about mixed-type interferometers using both amplitude- and wavefront-dividing beamsplitters in 2014 at the Tonomura FIRST Meeting. Toshiaki Tanigaki and I concieved the original idea and developed the experimental setup with hands-on guidance from Toshiaki and through helpful conversations and meetings with Ken Harada, Daisuke Shindo Benjamin McMorran and Hiroyuki Shinada. I fabricated the grating beamsplitters used, built scanning mode into the Hitachi TEM with help from Toshiaki, recorded all data, generated all figures, and wrote the supplemental material manuscript with input from coauthors.

Introduction to A tunable path-separated electron interferometer with an amplitude-dividing grating beamsplitter

Electron interferometry has been utilized to probe fundamental physics and provide object wave imaging since Dennis Gabor hypothesized an 'electron interference microscope' in 1948 [4]. Electrons offer different advantages from their optical counterparts. Electrons are massive, yet can still be accelerated to relativistic speeds. Their charge allows for a strong coupling to electromagnetic fields and their shorter De Broglie wavelength provides electron interferometers with higher resolving power, making them potent tools for materials research and the exploration of fundamental physics.

Marton et al. built the first electron interferometer using amplitude-dividing polycrystalline epitaxially grown copper membrane diffraction gratings in 1953 [74] and Möllenstedt et al. followed close behind with wavefront-dividing electron biprisms in 1955 [6]. The latter technology proved to be quite versatile allowing Lichte, Tonomura, Matteucci, Pozzi and many others to establish electron holography as a trusted technique for either high precision imaging [8, 9, 10, 11, 75] or probing basic physics [12, 13, 14]. Tanigaki *et al.* expanded on this setup through split-illumination electron holography (SIEH) [76], which boasts an additional two biprisms for pre-specimen beam splitting. This method utilizes the electron biprism to tune the path separation at the specimen plane, although with two notable difficulties. First, SIEH uses plane wave illumination incident on the specimen, similar to normal off-axis electron holography. This requires custom beam-blocking apertures in order to measure a field-of-interest surrounding a beam-sensitive specimen [77]. Second, although it remains a useful technology, Möllenstedt electron biprisms require wide, coherent incident beams when employed as a beamsplitter, thus demanding a highly coherent beam.

One way to alleviate this coherence requirement is by using electron diffraction grating beamsplitters. Similar to Marton et al.'s original beamsplitter, diffraction gratings are advantageous because they are amplitude-dividing beamsplitters, which create copies of the original wavefront propagating in different directions. They have the advantage that only a few grating bars, typically tens to hundreds of nanometers in pitch, must be coherently illuminated in order to maintain fringe visibility in the interference pattern [7, 78, 79]. This decreases the coherence width requirements by at least an order-of-magnitude when compared to current biprism beamsplitters, and could potentially allow implementation of this interferometer without highly coherent electron source guns such as cold field-emission guns or Schottky sources, for example. Holographic diffraction gratings have been developed by several groups [20, 21, 40, 45, 46, 47] and have been employed as beamsplitters in a couple of path separated electron interferometers [40, 53] and in a proposed electron interferometer with path separations of 10^{-2} m [80]. Using current focused ion beam (FIB) engineering techniques, we fabricated gratings that form electron diffraction orders (henceforth called p_n for the n_{th} order) with a spatial separation of hundreds of nanometers at the Lorentz sample plane, located in a field-free region above the objective lens useful for imaging magnetic materials, and tens of nanometers at the high-resolution sample plane in a commercial transmission electron microscope (TEM) configured in scanning (STEM) mode [53].

In this article, we combine an amplitude-dividing beamsplitter with the versatility of electrostatic biprisms to create a tunable path-separated electron interferometer. Harvey et al. and Yasin et al. previously developed and demonstrated full object wave measurement using STEM holography (STEMH) [81, 82]. Here, we use this interferometer to perform flexible STEM holography (fSTEMH), where we have increased flexibility via the tunability of the path separation. This increases the field of view of STEMH and opens the door to fundamental physics experiments as well as microscopy applications requiring large path-separations and localized-probe.

Experimental Setup

This interferometer was setup within a Hitachi HF-3000X TEM equipped with a cold field-emission gun and several positionable electrostatic biprism wires placed both pre- and post-specimen. As illustrated in Figure 14, the input electron wave diffracts through a diffraction grating with pitch $d = 190$ nm and is focused into electron probes with an estimated convergence semi-angle of 0.2 mrad and hundreds of nanometers spatial separation at the Lorentz specimen plane using a two-condenser lens illumination system. Note that the original probe separation at the specimen plane depends on both the physical pitch of the diffraction grating as well as the setup of the microscope lens system and biprisms. These gratings can be fabricated so that the amplitude of the diffraction orders other than p_{-1}, p_0 and p_{+1} are approximately negligible [21].

Four BPs are positioned along the optical axis and are tuned such that the diffraction probes straddle the three BPs located further down the microscope column. The probes are focused onto the first bi-prism (BP1), which blocks p_0 entirely. This increases the signal-to-noise of the desired frequency fringes for two reasons. First, the probe intensity $|p_0|^2 > |p_{n>0}|^2$, so it contains the majority of inelastically scattered electrons from the grating. Second, when p_{-1}, p_0 and p_{+1} are all utilized, the amplitude $|p_0|$ may be large enough for a non-negligible interference signal with

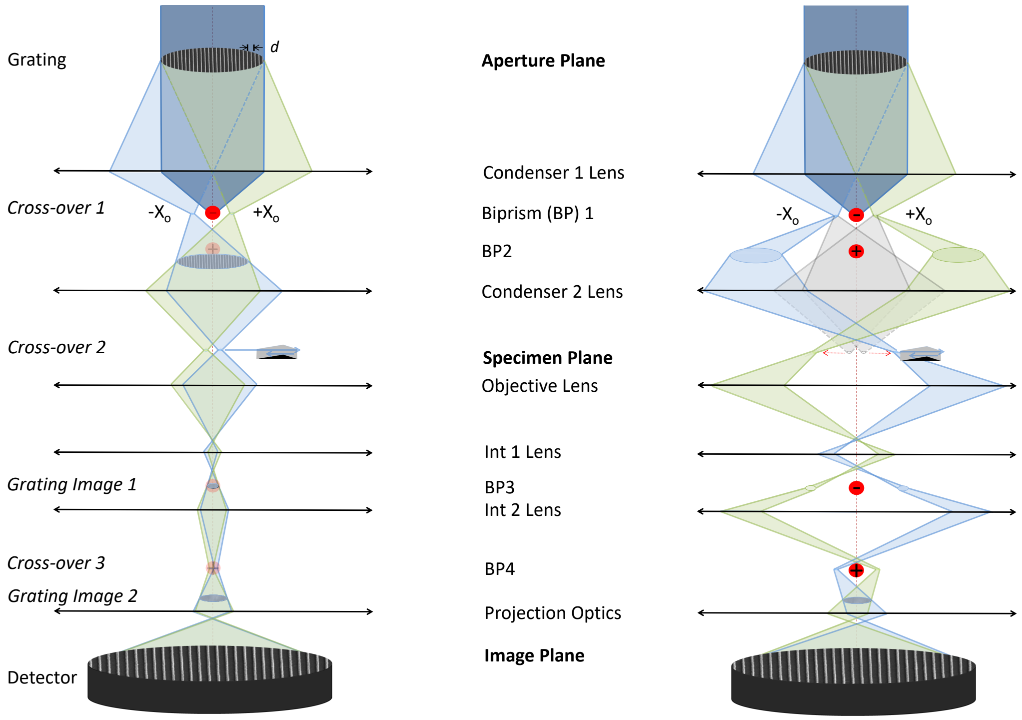

FIGURE 14. Experimental setup for a tunable path-separated interferometer. The right-hand-side illustrates the change in path with the biprisms engaged.

$p_{\pm 2}$, adding noise [82]. Blocking p_0 removes these two sources of noise. While the diffracted probes may contain inelastic scattering, Shiloh et al. has shown that a 200 nm thick SiN membrane has a ratio of elastic to inelastically scattered electrons of ≈ 0.66, with most of the inelastically scattered electrons contained in the long tails of the probes [83]. Since our diffraction grating is 75 nm thick, we expect the proportion of inelastically scattered electrons to be even lower. BP1 changes the overlap of the interference fringe discs while BP2 tunes the path separation of the probes in the specimen plane. BP1 and BP2 are tuned such that the remaining diffraction probes straddle BP2 and spatially separate at the specimen plane to a desired value. p_{-1} interacts with the phase-object while p_{+1} passes through vacuum. The image of the grating is then focused onto BP3, with two spatially separated images formed due to the voltage bias engaged in BP1. We tuned this voltage so that

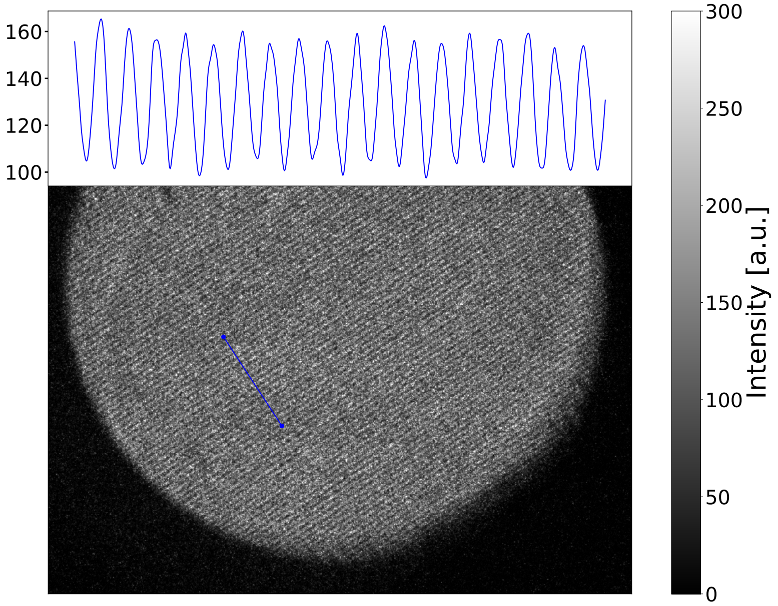

FIGURE 15. Interference fringes at the detector. Inset is the mean of 400 1D slices of the interference fringe pattern.

the images straddle BP3. We then engage BP3 to decrease the spatial separation of the diffraction probes focused onto BP4 in the reciprocal plane, affectively increasing the fringe spacing in the image plane at the detector. Finally, we engage BP4 to overlap the grating images onto the detector, a Gatan US4000 charge-coupled device (CCD) that records the interference pattern, shown in Figure 15.

Results

fSTEMH phase reconstructions of Si ramp

For use as an easily-characterizable phase object specimen, we placed Si on a Mo substrate with W as an adhesion layer using FIB microsampling [84]. We nanofabricated the Si to form a linear phase ramp, increasing from vacuum to ≈ 30 rad, (≈ 360 nm thick) over ≈ 1.2 μm on one side and decreases linearly with twice the gradient on the other side, or $-50\ \frac{\text{rad}}{\mu\text{m}}$. We performed both fSTEMH with a path separation of $\Delta x = 5\ \mu$m and off-axis electron holography on this test specimen. As shown in Figure 16, fSTEMH accurately measures the phase profile of the Si, as compared to off-axis electron holography.

The microscope we used wasn't outfitted with a native STEM mode or aberration correction, so the probe width at the specimen plane limits our resolution to ≈ 45 nm. A dedicated STEM can improve this resolution, and STEM holography has been previously demonstrated at subnanometer resolution [82]. We adjusted our scan step size to be as large as the probe width to decrease acquisition time, maximize beam stability and minimize data size. Due to undersampling, the phase image is pixelated, but contains quantitative amplitude and phase information that compares well to the off-axis electron holography reconstruction. Since we weren't using a fast-readout detector, the scan time was quite large as each pixel in Figures 16c and 16d corresponds to an ≈ 5 s dwell time. The beam current decreased over time, resulting in a decrease in the measured amplitude as seen in Figure 16d from the start of the scan (bottom left) to the end (upper right). This decrease notably does not affect the phase image in Figure 16c, and isn't present in previous STEMH data sets that utilize a fast readout detector [81, 82].

Fringe visibility versus path separation

In order to determine a range of path separations usable by such an interferometer under these experimental conditions and limit any noise from higher order diffraction probes, we fabricated an aperture with a series of two-slit windows (Figure S.4. in the supplemental materials with well defined, varied path separations. We used this aperture to isolate p_{+1} and p_{-1} at the specimen plane and measure the fringe visibility $\mathcal{V}$ of the interference fringes at the detector over a range of path separations Δx.

We adjusted BP2 to set Δx, BP3 and BP4 to maintain a constant fringe spacing $d_I \approx 147$ μm, and held BP1$= -100$ V and all lens values constant throughout. Images of the probes for a selection of path separations and their corresponding averaged, normalized interference fringe profiles are shown in Figure 17.

The results are shown in Figure 18. $\mathcal{V}\left(\Delta x\right)$ increases until $\Delta x \approx 4$ μm, after which it decreases monotonically. This decrease in $\mathcal{V}$ can be explained by stray magnetic fields passing through the area enclosed by the interferometer. According to the Aharanov-Bohm effect, the phase difference between two paths of an electron interferometer depends linearly on both the area enclosed by the two paths, A, and the time-dependent alternating current (AC) stray magnetic field, $B(t)$. This introduces a time dependent phase in the interference fringes at the detector, modeled as $B(t) = B_0 sin(\omega t)$.

Here, the interferometer has four enclosed areas. Referring to Figure 19, A_1 encloses BP2, A_2 is located at the objective lens, A_3 is located at the intermediate 1 lens and A_4 encloses BP3. This results in four independent phase terms that affect the interference fringes recorded for a finite time interval, or 2 s for this experiment.

This time average has a couple of consequences. First, it is a source of noise that decreases the fringe visibility of the interferometer at the onset. Second, increasing A_n increases the amplitude of these phase fluctuations without changing the frequency. When time averaged over the same 2 s time interval, destructive interference decreases the fringe visibility to a minimum.

Initially, BP2 and BP3 are not engaged, and so the path separation at the Lorentz sample position is $\Delta x = 1.9$ μm. As BP2 is engaged and increased in value, A_1 begins to decrease. We measure an increase in $\mathcal{V}$ for these first changes in BP2, 3 and 4. This could be explained by the stochastic fluctuations of the amplitude and frequency of the thermal magnetic field noise, as described and demonstrated previously by Uhlemann et al [85]. A_1 is initially large, suggesting that fluctuations in B_1 and ω_1 dominate the phase fluctuations. As A_1 decreases, these phase fluctuations decrease, suggesting that the fringe visibility increases due to more constructive interference over the 2 s exposure. Simultaneously, $A_{n>1}$ all increase in magnitude, suggesting that there must also be an eventual decrease in $\mathcal{V}$ as the path separation increases. This increase in $A_{n>1}$ would explain the decrease in $\mathcal{V}$ for $\Delta x > 3.8$ μm. We simulated this fringe visibility experiment with thermal magnetic field fluctuations and present the results in the supplemental materials in Figure S.3.

To test the largest path separation possible, we increased the path separation to $\Delta x = 25$ μm. However, due to considerations of the voltage that can be applied to BP3 safely, this path separation could only be achieved at a much smaller fringe spacing, $d_I \approx 30$ μm. This spacing corresponds to the Nyquist frequency of the detector, which results in an expected decrease in $\mathcal{V}$. We measured $\mathcal{V} = 0.67\% \pm 0.15\%$ under these conditions as shown in the supplemental materials.

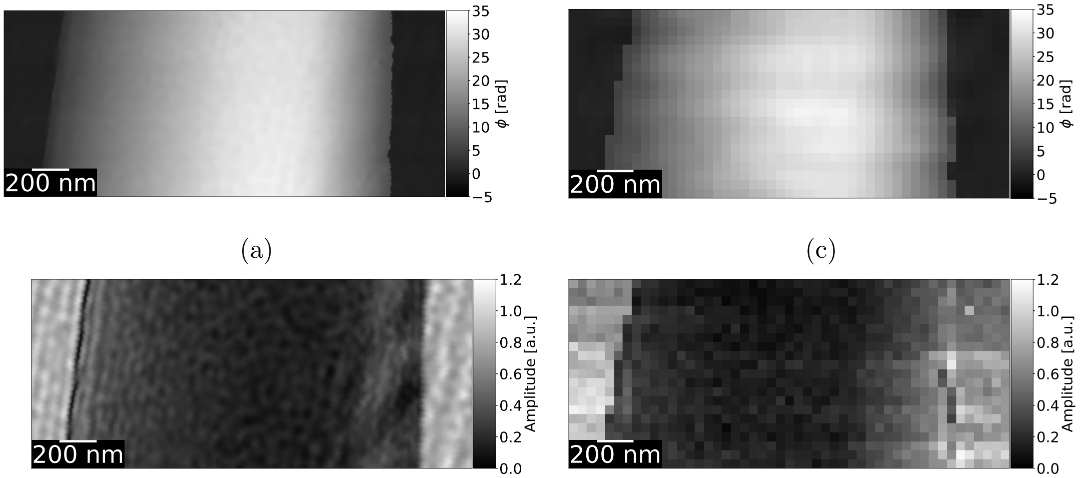

(a) (c)

(b) (d)

FIGURE 16. fSTEMH image of a fabricated Si phase ramp that increases linearly from vacuum with a gradient of 25 $\frac{\text{rad}}{\mu\text{m}}$ on one side and decreases linearly with twice the gradient on the other side $\left(-50\ \frac{\text{rad}}{\mu\text{m}}\right)$. (a,b) The reconstructed unwrapped phase image as well as the amplitude of the object wave using conventional off-axis electron holography. (c,d) Same as (a,b), but using fSTEMH with $\Delta x = 5\ \mu\text{m}$.

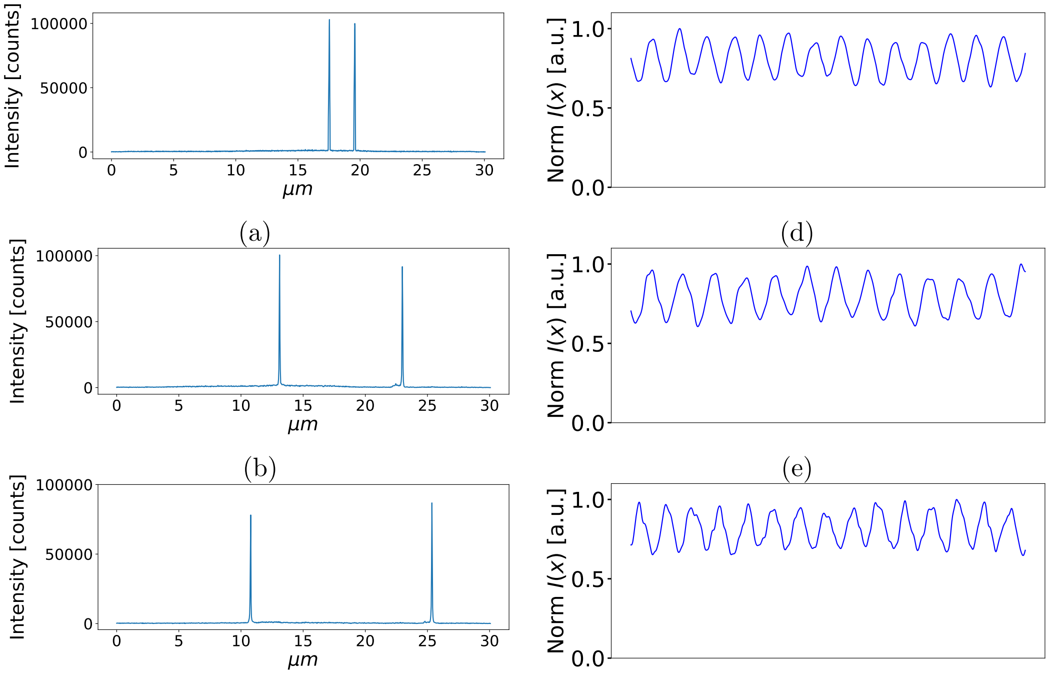

(a) (d)

(b) (e)

(c) (f)

FIGURE 17. (a-c) 1D profile of p_{+1} and p_{-1} in vacuum with a two slit window aperture inserted in the sample position to block all higher diffraction orders. (d-f) Interference fringes acquired over a 10 s exposure for the corresponding path separations shown in (a-c).

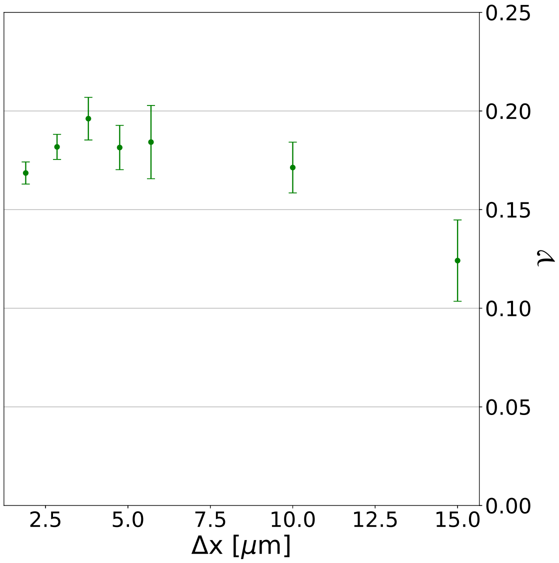

FIGURE 18. Interference fringe visibility versus path separation length between the electron probes at the specimen plane.

Discussion

The BPs allow for increased flexibility in multiple ways. The ability to tune the path separation to arbitrarily large values at the specimen plane enables large-geometry electron interferometry experiments. For example, studies of forward-scattering due to atoms or molecules located in an isolated gas cell [86], the nature of the Aharonov-Bohm effect from an isolated solenoid [87, 88], decoherence theory and the quantum-classical boundary as the delocalized probe entagles with the environment, and enclosing the arms of a charged particle interferometer in a Faraday cage for rotation sensing [89] could all be enabled by this setup. Additionally, fSTEMH may enable quantitative phase mapping with respect to vacuum of programmable phase plates such as the ones proposed by Verbeeck et al. [90]. Each of the above experiments requires either a large spatial separation between interferometer arms in order to place a physical boundary between the two, or the ability to tune the path separation over a significant range of values. fSTEMH provides such an interferometric setup.

Furthermore, fSTEMH independently positions the localised reference beam anywhere in a small area of the specimen, whereas conventional TEM holography requires that one wide reference field pass through vacuum outside of the sample, which places limits on the types of specimen geometries that can be imaged. Finally, the use of a holographic beamsplitter allows additional control over the electron beam, such as removing the spherical aberration [68] or introducing phase vortices that can be used to measure magnetic fields [91].

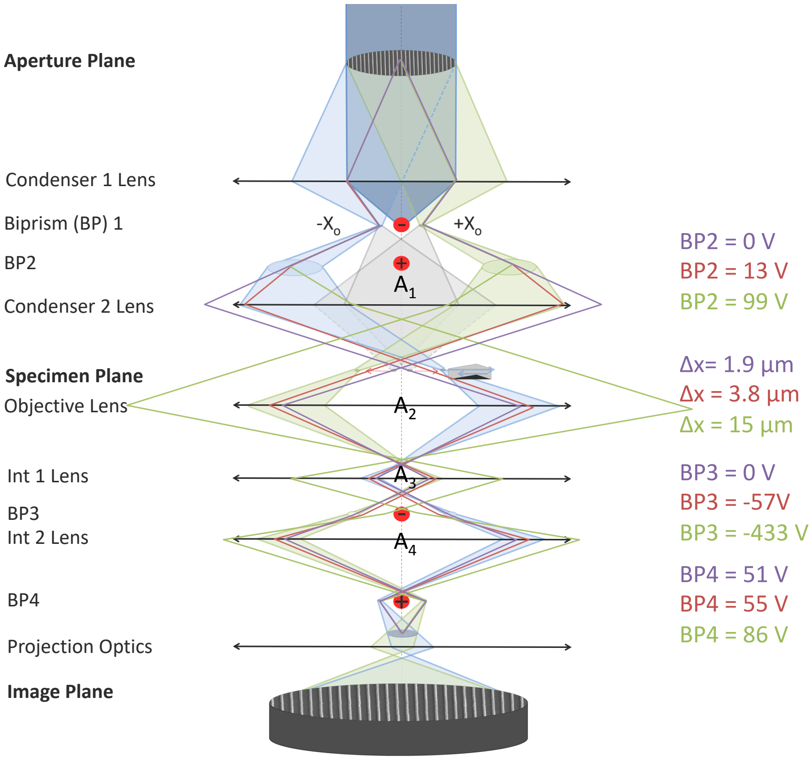

FIGURE 19. fSTEMH setup for different path separations. Notice the change in the enclosed areas A_1, A_2, A_3 and A_4. As the path separation increases initially, the total area enclosed decreases, but then increases monotonically, leading to a loss in fringe visibility for very large path separations.

Conclusion

We demonstrate a tunable path-separated electron interferometer within a STEM. We use a nanofabricated grating as an amplitude-dividing beamsplitter capable of preparing multiple spatially separated, coherent electron probe beams with 950 nm spatial separation between neighbor diffraction orders at the specimen. We configure four electrostatic bi-prisms (BPs) down the optical column and tune the voltage applied to each to achieve path separations between p_{+1} and p_{-1} at the specimen plane of up to 25 μm while maintaining fringe visibility at the detector.

We performed fSTEMH on a Si test specimen with the path separation tuned to 5.0 μm. We measure highly interpretable, quantitative amplitude and phase contrast that agrees with an independent measurement using off-axis electron holography. We measure the fringe visibility of this interferometer over a range of path separations to establish the interferometer's utility at large path separations. This experimental design can potentially be applied to phase imaging and fundamental physics experiments, such as the Aharonov-Bohm effect, decoherence theory and electromagnetic field mapping around a specimen's edge without exposing the specimen to radiation.

$\mathcal{V}$ versus area enclosed by interferometer

Theory

As stated in many textbooks and review papers (see [92, 93], for example), the phase between two arms of an electron interferometer depends on a magnetic field **B** normal to the area **S** enclosed by the interferometer as

$$\phi_2 - \phi_1 = \frac{2\pi e}{h} \int_{\mathbf{S}} \mathbf{B} \cdot d\mathbf{S}, \tag{4.1}$$

where h is Planck's constant, e is the elementary electric charge and **S** denotes the perimeter of the interferometer. Note that stray alternating current **B** field depends on time and points orthogonal to the local area enclosed, $\mathbf{B} \cdot \mathbf{S} = B_\perp(t)A$. This reduces equation (4.1) to

$$\Delta\phi = -\frac{2\pi e}{h} B_\perp(t)A, \tag{4.2}$$

where A is the area enclosed by the two paths and $B_\perp(t) = B_0 sin(\omega t)$. The amplitude B_0 and frequency ω of the stray fields fluctuate at each time increment dt. To simulate thermal fluctuations in the magnetic field, we will treat each amplitude and frequency term as a mean $\bar{B}_0 = 1$ nT$, \bar{\omega} = 5$ kHz and stochastically vary each independently from a gaussian distribution.

In this experimental setup, there are four enclosed areas. Due to beam crossovers between each area, the phase difference as electrons propagate around A_1 and A_3 accumulates in the opposite direction as when they propagate around A_2 and A_4. However, due to rotation in the beam around the optical axis as the beam travels down the column, the normal vector of each area points in a unique direction. Additionally, we expect thermal magnetic field noise to be a main contributor to the stray fields penetrating these areas as previously studied and demonstrated by Uhlemann et al [85]. These fields not only fluctuate in time, but depend on z as well. Therefore, we treat the magnetic field within each area as uniform, but local to each area.

For a 2-beam interferometer, like the one employed using the 2-slit aperture shown in Figure 23 to block all higher order diffraction probes, the intensity pattern at the detector is

$$I(\mathbf{x}) = I_0 + c_{-1}^{*} c_{+1} e^{\left(i \sum_{n=1}^{4} \Delta\phi_n\right)} e^{\left(-2\pi i \frac{\mathbf{x}}{d_I}\right)} + c_{-1} c_{+1}^{*} e^{\left(-i \sum_{n=1}^{4} \Delta\phi_n\right)} e^{\left(2\pi i \frac{\mathbf{x}}{d_I}\right)}, \tag{4.3}$$

where c_m is the complex amplitude of the m^{th} electron diffraction probe beam, $I_0 = |c_{-1}|^2 + |c_{+1}|^2$, d_I is the fringe spacing, and $\Delta\phi_n$ is the magnetic phase difference acquired around the n^{th} area. Setting $c_m = \frac{1}{2}$ for ease, expanding $\Delta\phi_n$ and time averaging over a t_f [**s**] exposure,

$$\bar{I}(\mathbf{x}, A_n) = \int_0^{t_f} \left[I_0 + \frac{1}{2} cos \left(\frac{\mathbf{x}}{d_I} + \frac{2\pi e}{h} \sum_{n=1}^{4} (-1)^n A_n \bar{B}_n sin(\bar{\omega}_n t) \right) \right] dt \tag{4.4}$$

We know fringe visibility is defined as

$$\mathcal{V} = \frac{I_{max} - I_{min}}{I_{max} + I_{min}}. \tag{4.5}$$

Experiment and simulation

Using this definition, we can simulate multiple time averaged (2 s exposure) interference patterns as a function of A and calculate $\mathcal{V}$ for each. As seen in Figure

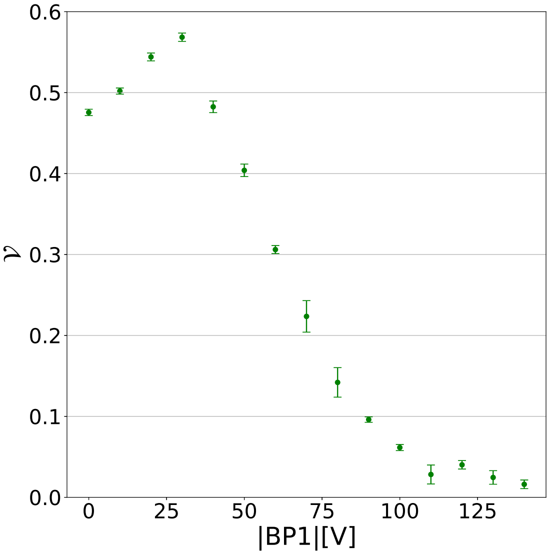

FIGURE 20. Experimentally measured interference fringe visibility versus the biprism 1 voltage applied, the absolute value of which is proportional to the area enclosed by the interferometer.

19 in the main text, all enclosed areas A_n of the interferometer increase for decreasing the voltage in BP1, or increasing $|BP1|$. Therefore, we performed an experiment and simulation, decreasing the BP1 voltage, which increases A_n, while increasing BP4 to maintain an overlap of the interference fringes at the detector. As shown in Figure 20, a decrease in the BP1 voltage results in a decrease in fringe visibility $\mathcal{V}$. Note that this is not the same as Figure 18, which plots $\mathcal{V}$ versus the path separation of the probes at the specimen plane.

We simulated Gaussian stochastic fluctuations over various standard deviations in both the amplitude B_0 and frequency ω using an average $\bar{B}_0 = 1$ nT and two mean frequencies $\bar{\omega} = 5$ kHz and $\bar{\omega} = 5$ MHz, representing the range of frequencies expected for the field noise [85]. We included Poissonian shot noise and used fringe spacing $d_I = 147$ μm. The resulting simulated plots are shown in Figure 21. They

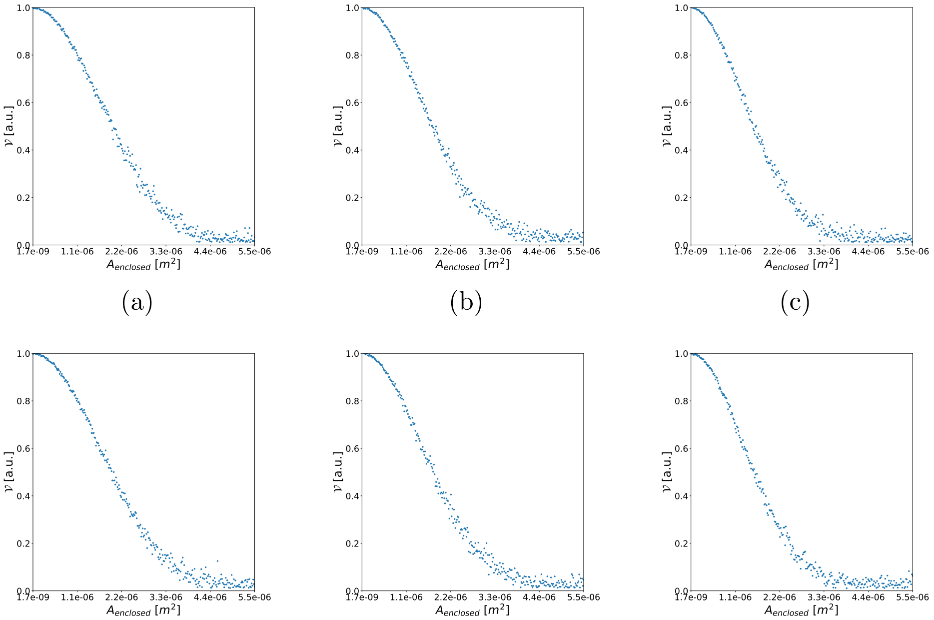

(a) (b) (c)

(d) (e) (f)

FIGURE 21. Simulated $\mathcal{V}(A)$ for $\bar{\omega} = 5$ kHz and a) $\sigma_{B_0} = \frac{5}{10}\bar{B}_0$, $\sigma_\omega = \frac{5}{10}\bar{\omega}$, b) $\sigma_{B_0} = \frac{7.5}{10}\bar{B}_0$, $\sigma_\omega = \frac{7.5}{10}\bar{\omega}$, c) $\sigma_B = \bar{B}_0$, $\sigma_\omega = \bar{\omega}$, d-f) same as a-c) except with $\bar{\omega} = 5$ MHz.

were calculated using simulated interference fringes from equation 4.4. As seen in Figure 21, $\mathcal{V}$ decreases with A for each standard deviation.

Fringe visibility versus path separation simulation

As shown in Figure 18 in the main text, $\mathcal{V}(A_n)$ increases initially before monotonically decreasing. We explained this phenomena as being due to a decreasing A_1 while $A_{n>1}$ increases. To simulate this, we set A_1 to decrease linearly from 0.83 μm^2 to 0.083 μm^2 while $A_{n>1}$ increase linearly from 0.083 μm^2 to 0.83 μm^2. These values are a rough Fermi estimate of $A_n \approx \Delta x * L$, where the length between crossovers $L \approx 10^{-1}$ m The results are shown in Figure 22. The curve follows a similar qualitative trend as Figure 18.

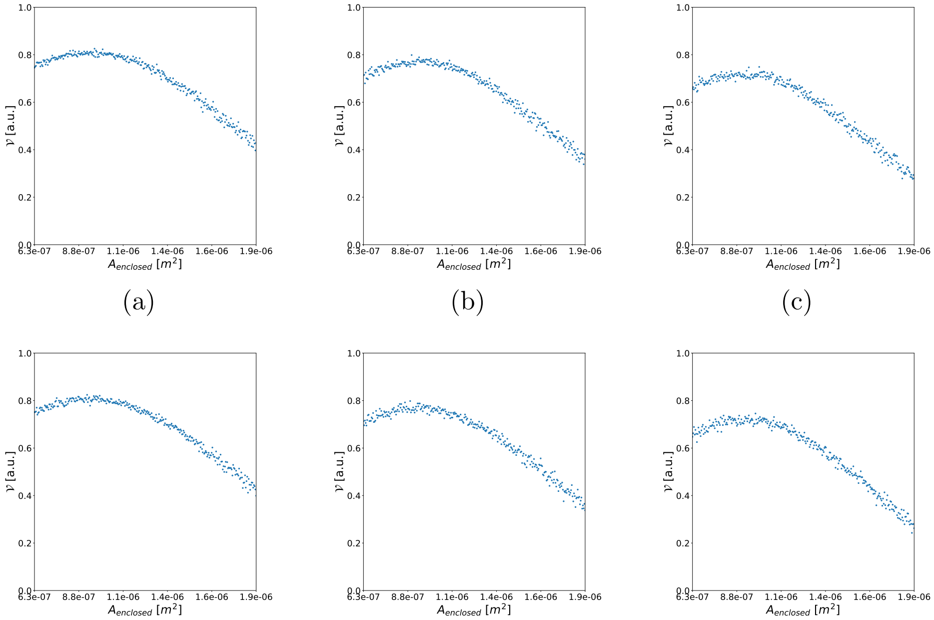

(a) (b) (c)

(d) (e) (f)

FIGURE 22. Simulated $\mathcal{V}(A)$ for increasing A_1 and decreasing $A_{n>1}$, which corresponds to an increasing path separation at the sample plane. For a-c) $\bar{\omega} = 5$ kHz. a) $\sigma_{B_0} = \frac{5}{10}\bar{B}_0$, $\sigma_\omega = \frac{5}{10}\bar{\omega}$, b) $\sigma_{B_0} = \frac{7.5}{10}\bar{B}_0$, $\sigma_\omega = \frac{7.5}{10}\bar{\omega}$, c) $\sigma_B = \bar{B}_0$, $\sigma_\omega = \bar{\omega}$, d-f) same as a-c) except with $\bar{\omega} = 5$ MHz.

Additional figures

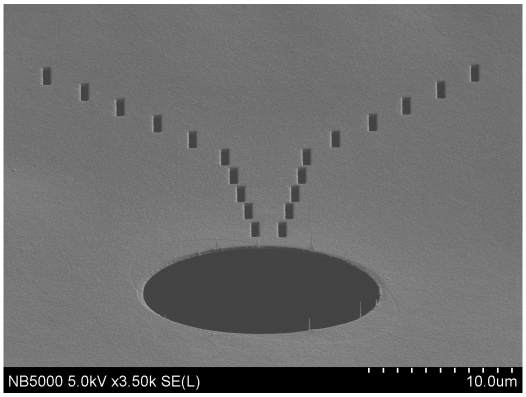

FIGURE 23. Scanning electron microscopy micrograph of the two-slit aperture used to block the higher order diffraction probes while performing the fringe visibility versus path separation experiment described in the main text.

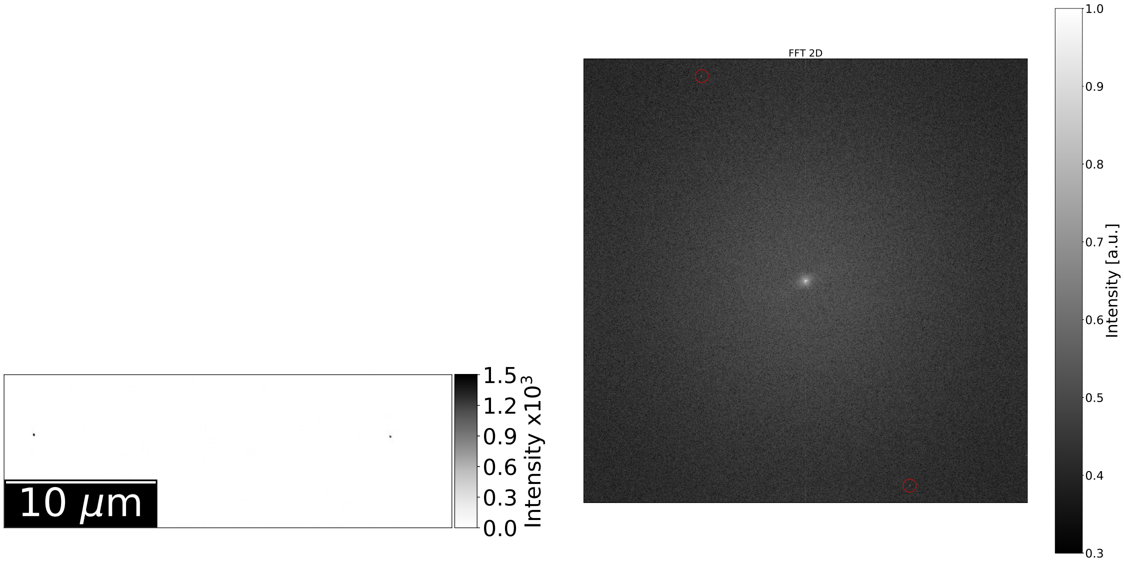

(a) (b)

FIGURE 24. a) An image of the diffraction probes at the specimen plane with $\Delta x = 25$ μm. b) An image of the Fourier transform of the interference fringes with the peaks corresponding to the fringe spacing circled in red.

Chapter Conclusion

In this chapter we demonstrated a tunable path-separated electron interferometer with the largest demonstrated path separations for amplitude-dividing electron interferometers. Such large path separations enable large field of view STEMH imaging as well as large geometry physics experiments such as an exploration of the Aharonov-Bohm effect or imaging the electric and magnetic near fields around a beam-sensitive object without exposing the object to radiation. Additionally, the addition of a direct beam-blocking biprism coupled with a prespecimen two-slit aperture to block higher diffraction-order beams allows all electrons illuminating the specimen to be used to form the signal in the interference fringe pattern, potentially making fSTEMH the most dose-efficient form of electron holography available. This dose-efficiency would essentially be limited by inelastic scattering to the p_{+1} and p_{-1}.

CHAPTER V

CONCLUSION AND FUTURE DIRECTIONS

We demonstrated that STEMH may be used as both a practical atomic resolution phase-contrast imaging technique and a tunable electron interferometer capable of probing basic physics. As an imaging technique, we achieved atomic resolution of multiple gold nanoparticles on an ultra-thin carbon substrate. We were able to confirm a unique, non-random carbon bond structure in the thin substrates, while resolving the gold atomic lattice with the same resolution as the simultaneously acquired conventional STEM HAADF images. We were also able to expand the initially proposed setup using four electrostatic biprisms, two pre- and two post-specimen, into a tunable electron interferometer. We showed that fSTEMH remains a quantitative imaging technique capable of both phase and amplitude contrast in this experimental setup, and were able to explore the nature of the magnetic field noise incident on such an interferometer as predicted and modeled by Uhlemann et al [85].

We adapted this interferometric setup into multiple electron microscopes in two different countries including a Thermo Fisher Titan 80-300 KV TEM with STEM capabilities located within the Center for Advanced Materials Characterization in Oregon at the University of Oregon, a Thermo Fisher Titan 80-300 kV TEM with STEM capabilities, probe and image aberration correction and a Gatan K2 Summit direct electron detector located within the National Center for Electron Microscopy at Lawrence Berkeley National Laboratory, and finally a Hitachi HF-3000X TEM equipped with a cold field-emission gun and several positionable electrostatic biprism wires placed both pre- and post-specimen. These rapid installations are a testament to the utility and flexibility that comes with using nanofabricated diffraction gratings as the beamsplitter within the experimental setup. The ease-of-installation, scalability and low cost of these grating beamsplitters could enable scanning transmission electron microscopes around the world to have a working, quantitative imaging technique for electron transparent "phase" materials and nanomaterials of interest within the semiconductor industry, especially those with lesser known electro-magnetic field distributions.

In addition to the benefits of having such an imaging technique as STEMH, we are excited for the potential of developing STEMH as a quantum electron interferometric imaging technique, which could potentially lower the dose incident on specimens by a couple order of magnitudes, enabling quatitative, non-destructive biological imaging applications. While such imaging may not be currently possible, future technologies such as faster readout cameras and higher efficiency amplitude-dividing beamsplitters might allow for such a low dose while maintaining fringe visibility at the detector. The addition of a path separation tuning knob within fSTEMH enables the probing of new sample geometries and electro-magnetic fields in or around specimens of interest. It also enables interesting quantum "which way" experiments, and may lead to interesting insights and a greater understanding of an electron quantum wavefunction.

REFERENCES CITED

[1] F. Zernike. Phase contrast, a new method for the microscopic observation of transparent objects. *Physica*, 9(7):686 – 698, 1942.

[2] M. J. Holland and K. Burnett. Interferometric detection of optical phase shifts at the heisenberg limit. *Phys. Rev. Lett.*, 71:1355–1358, Aug 1993.

[3] B. P. Abbott et al. Observation of gravitational waves from a binary black hole merger. *Phys. Rev. Lett.*, 116:061102, Feb 2016.

[4] D. Gabor. A new microscopic principle. *Nature*, 161:777–8, 1948.

[5] L. Marton, J. Arol Simpson, and J. A. Suddeth. Electron beam interferometer. *Physical Review*, 90(3):490–491, 1953.

[6] G. Möllenstedt and H. Düker. Fresnelscher Interferenzversuch mit einem Biprisma für Elektronenwellen. *Naturwissenschaften*, 42:41–41, jan 1955.

[7] G. Matteucci, G.F. Missiroli, and G. Pozzi. Amplitude division electron interferometry. *Ultramicroscopy*, 6:109–114, 1981.

[8] G. Pozzi. Off-axis image electron holography with a mixed type interferometer. *Optik*, 63:227–38, 1983.

[9] H Lichte. Electron image plane off-axis holography of atomic structures. *Advances in optical and electron microscopy*, 12:25–91, 1991.

[10] Akira Tonomura. *Electron Holography.* Springer-Verlag Berlin Heidelberg, 1993.

[11] Hannes Lichte, Dorin Geiger, and Martin Linck. Off-axis electron holography in an aberration-corrected transmission electron microscope. *Philosophical Transactions of the Royal Society of London A: Mathematical, Physical and Engineering Sciences*, 367(1903):3773–3793, 2009.

[12] G. Matteucci and G. Pozzi. New diffraction experiment on the electrostatic aharanov-bohm effect. *Physical Review Letters*, 54(23):2469–2472, 1985.

[13] A. Tonomura, N. Osakabe, T. Matsuda, T. Kawasaki, and J. Endo. Evidence for aharanov-bohm effect with magnetic field completely shielded from electron wave. *Physical Review Letters*, 56(8):792–795, 1986.

[14] H. Lichte and M. Lehmann. Electron holography - basics and applications. *Rep. Prog. Phys.*, 71(016102), 2008.

[15] Giulio Pozzi, Marco Beleggia, Takeshi Kasama, and Rafal E. Dunin-Borkowski. Interferometric methods for mapping static electric and magnetic fields. *Comptes Rendus Physique*, 15:126–139, 2014.

[16] Th. Leuthner, H. Lichte, and K.-H. Herrmann. Stem-holography using the electron biprism. *physica status solidi (a)*, 116(1):113–121, 1989.

[17] J.M. Cowley. High resolution side-band holography with a stem instrument. *Ultramicroscopy*, 34:293 – 297, 1990.

[18] Yoshio Takahashi, Yusuke Yajima, Masakazu Ichikawa, and Katsuhiro Kuroda. Observation of magnetic induction distribution by scanning interference electron microscopy. *Japanese Journal of Applied Physics*, 33(9B):L1352, 1994.

[19] J.M. Cowley. Ultra-high resolution with off-axis stem holography. *Ultramicroscopy*, 96:163 – 166, 2003.

[20] B. J. McMorran, A. Agrawal, I. M. Anderson, A. A. Herzing, H. J. Lezec, J. J. McClelland, and J. Unguris. Electron vortex beams with high quanta of orbital angular momentum. *Science*, 331:192–195, 2011.

[21] T.R. Harvey, J.S. Pierce, A.K. Agrawal, P. Ercius, M. Linck, and B.J. McMorran. Efficient diffractive phase optics for electrons. *New Journal of Physics*, 16, 2014.

[22] J.M. Cowley. High resolution side-band holography with a stem instrument. *Ultramicroscopy*, 34:293 – 297, 1990.

[23] M. E. Haine and T. Mulvey. The formation of the diffraction image with electrons in the gabor diffraction microscope. *J. Opt. Soc. Am.*, 42(10):763–773, Oct 1952.

[24] Tatiana Latychevskaia and Hans-Werner Fink. Solution to the twin image problem in holography. *Phys. Rev. Lett.*, 98:233901, Jun 2007.

[25] Manuel Guizar-Sicairos and James R. Fienup. Understanding the twin-image problem in phase retrieval. *J. Opt. Soc. Am. A*, 29(11):2367–2375, Nov 2012.

[26] Herbert Wahl. *Bildebenenholographie mit Elektronen.* [s.n.], [S.l.], 1975.

[27] Emmett N. Leith and Juris Upatnieks. Reconstructed wavefronts and communication theory∗. *J. Opt. Soc. Am.*, 52(10):1123–1130, Oct 1962.

[28] G. Möllenstedt and H. Düker. Beobachtungen und messungen an biprisma-interferenzen mit elektronenwellen. *Zeitschrift für Physik*, 145(3):377–397, 1956.

[29] K.-J. Hanszen. Holography in electron microscopy. In Peter W. Hawkes, editor, *Advances in Electronics and Electron Physics*, volume 59 of *Advances in Electronics and Electron Physics*, pages 1 – 77. Academic Press, 1982.

[30] Martha R. McCartney and David J. Smith. Electron holography: Phase imaging with nanometer resolution. *Annual Review of Materials Research*, 37(1):729–767, 2007.

[31] Paul A. Midgley and Rafal E. Dunin-Borkowski. Electron tomography and holography in materials science. *Nature Materials*, 8(4):271–280, April 2009.

[32] Martin Hÿtch, Florent Houdellier, Florian Hüe, and Etienne Snoeck. Nanoscale holographic interferometry for strain measurements in electronic devices. *Nature*, 453(7198):1086–1089, June 2008.

[33] David Cooper, Cheng-Ta Pan, and Sarah Haigh. Atomic resolution electrostatic potential mapping of graphene sheets by off-axis electron holography. *Journal of Applied Physics*, 115(23), 2014.

[34] G. Matteucci, G. F. Missiroli, and G. Pozzi. Amplitude division electron interferometry. *Ultramicroscopy*, 6(2):109–113, 1981.

[35] Q. Ru, N. Osakabe, J. Endo, and A. Tonomura. Electron holography available in a non-biprism transmission electron microscope. *Ultramicroscopy*, 53(1):1–7, 1994.

[36] Fang Zhou. The principle of a double crystal electron interferometer. *Journal of Electron Microscopy*, 50(5):371–376, 2001.

[37] A. Agarwal, C-S. Kim, R. Hobbs, D. van Dyck, and K.K. Berggren. A nanofabricated, monolithic, path-separated electron interferometer. *Scientific Reports*, 7(1677), 2017.

[38] L. Marton. Electron interferometer. *Physical Review*, 85(6):1057–1058, 1952. 00125.

[39] L. Marton, J. Arol Simpson, and J. A. Suddeth. An electron interferometer. *Review of Scientific Instruments*, 25(11):1099, 1954. 00099.

[40] Glen Gronniger, Brett Barwick, Herman Batelaan, Tim Savas, Dave Pritchard, and Alex Cronin. Electron diffraction from free-standing, metal-coated transmission gratings. *Applied Physics Letters*, 87(12):124104, 2005.

[41] B.J. McMorran, T.A. Perreault, and A. Cronin. Diffraction of 0.5 kev electrons from free-standing transmission gratings. *Ultramicroscopy*, 106:356, 2006.

[42] G. Gronniger, B. Barwick, and H. Batelaan. A three-grating electron interferometer. *New Journal of Physics*, 8:224, 2006. 00011.

[43] B.J. McMorran and A. Cronin. An electron talbot interferometer. *New Journal of Physics*, 11:033021, 2009.

[44] Alexander Cronin and Ben McMorran. Electron interferometry with nanogratings. *Physical Review A*, 74(6):061602(R), 2006.

[45] J. Verbeeck, H. Tian, and P. Schattschneider. Production and application of electron vortex beams. *Nature*, 467:301–304, 2010.

[46] Roy Shiloh, Yossi Lereah, Yigal Lilach, and Ady Arie. Sculpturing the electron wave function using nanoscale phase masks. *Ultramicroscopy*, 144:26 – 31, 2014.

[47] Vincenzo Grillo, Gian Carlo Gazzadi, Ebrahim Karimi, Erfan Mafakheri, Robert W. Boyd, and Stefano Frabboni. Highly efficient electron vortex beams generated by nanofabricated phase holograms. *Applied Physics Letters*, 104(4):043109, January 2014.

[48] J.M. Cowley. Ultra-high resolution with off-axis stem holography. *Ultramicroscopy*, 96:163 – 166, 2003.

[49] P. D. Nellist and S. J. Pennycook. Incoherent imaging using dynamically scattered coherent electrons. *Ultramicroscopy*, 78:111–24, 1999.

[50] L. Reimer and H. Kohl. *Transmission Electron Microscopy Physics of Image Formation*. Springer Series in Optical Sciences. Springer Science+Business Media, LLC, New York, NY, fifth edition, 2008.

[51] Tyler R Harvey, Fehmi S Yasin, Jordan J Chess, Jordan S Pierce, Roberto M. S. dos Reis, Vasfi Burak Özdöl, Peter Ercius, Jim Ciston, Wenchun Feng, Nicholas A. Kotov, Benjamin J McMorran, and Colin Ophus. Interpretable and efficient contrast in scanning transmission electron microscopy with a diffraction-grating beam splitter. *Physical Review Applied*, 10(6):061001, 2018.

[52] T. Tanigaki, Y. Inada, S. Aizawa, T. Suzuki, H. Park, and T. Matsuda. Split-illumination electron holography. *Applied Physics Letters*, 101(4):043101, 2012.

[53] F.S. Yasin, T.R. Harvey, J. Chess, J.S. Pierce, and B.J. McMorran. Path-separated electron interferometry in a scanning transmission electron microscope. *Journal of Physics D: Applied Physics*, 2018.

[54] J. M. Rodenburg, B. C. McCallum, and P. D. Nellist. Experimental tests on double-resolution coherent imaging via STEM. *Ultramicroscopy*, 48(3):304–314, 1993.

[55] Timothy J. Pennycook, Andrew R. Lupini, Hao Yang, Matthew F. Murfitt, Lewys Jones, and Peter D. Nellist. Efficient phase contrast imaging in STEM using a pixelated detector. part 1: Experimental demonstration at atomic resolution. *Ultramicroscopy*, 151:160–167, 2015.

[56] H. Yang, R. N. Rutte, L. Jones, M. Simson, R. Sagawa, H. Ryll, M. Huth, T. J. Pennycook, M. L. H. Green, H. Soltau, Y. Kondo, B. G. Davis, and P. D. Nellist. Simultaneous atomic-resolution electron ptychography and Z-contrast imaging of light and heavy elements in complex nanostructures. *Nature Communications*, 7:12532, 2016.

[57] Hao Yang, Peter Ercius, Peter D. Nellist, and Colin Ophus. Enhanced phase contrast transfer using ptychography combined with a pre-specimen phase plate in a scanning transmission electron microscope. *Ultramicroscopy*, 171:117–125, 2016.

[58] Philipp Michael Pelz, Wen Xuan Qiu, Robert Bcker, Gnther Kassier, and R. J. Dwayne Miller. Low-dose cryo electron ptychography via non-convex bayesian optimization. *Scientific Reports*, 7(1):9883, 2017.

[59] Xueming Li, Paul Mooney, Shawn Zheng, Christopher R. Booth, Michael B. Braunfeld, Sander Gubbens, David A. Agard, and Yifan Cheng. Electron counting and beam-induced motion correction enable near-atomic-resolution single-particle cryo-EM. *Nature Methods*, 10(6):584–590, 2013.

[60] Michael Elbaum, Sharon G. Wolf, and Lothar Houben. Cryo-scanning transmission electron tomography of biological cells. *MRS Bulletin*, 41(7):542–548, 2016.

[61] Colin Ophus, Jim Ciston, Jordan Pierce, Tyler R. Harvey, Jordan Chess, Benjamin J. McMorran, Cory Czarnik, Harald H. Rose, and Peter Ercius. Efficient linear phase contrast in scanning transmission electron microscopy with matched illumination and detector interferometry. *Nature Communications*, 7:10719, 2016. 00014.

[62] M. R. McCartney, P. Kruit, A. H. Buist, and M. R. Scheinfein. Differential phase contrast in TEM. *Ultramicroscopy*, 65(3):179–186, 1996.

[63] Thibaud Denneulin, Florent Houdellier, and Martin Htch. Differential phase-contrast dark-field electron holography for strain mapping. *Ultramicroscopy*, 160:98–109, 2016.

[64] Shigeyuki Morishita, Ryo Ishikawa, Yuji Kohno, Hidetaka Sawada, Naoya Shibata, and Yuichi Ikuhara. Attainment of 40.5 pm spatial resolution using 300 kv scanning transmission electron microscope equipped with fifth-order aberration corrector. *Microscopy*, 67(1):46–50, 2018.

[65] Tetsuya Akashi, Yoshio Takahashi, Toshiaki Tanigaki, Tomokazu Shimakura, Takeshi Kawasaki, Tadao Furutsu, Hiroyuki Shinada, Heiko Mller, Maximilian Haider, Nobuyuki Osakabe, and Akira Tonomura. Aberration corrected 1.2-MV cold field-emission transmission electron microscope with a sub-50-pm resolution. *Applied Physics Letters*, 106(7):074101, February 2015.

[66] R.S. Ruskin, Z. Yu, and N. Grigorieff. Quantitative characterization of electron detectors for transmission electron microscopy. *Journal of structural biology*, 184(3), 2013.

[67] C. Ricolleau, Y. Le Bouar, H. Amara, O. Landon-Cardinal, and D. Alloyeau. Random vs realistic amorphous carbon models for high resolution microscopy and electron diffraction. *Journal of Applied Physics*, 114(21):213504, 2013.

[68] Martin Linck, Peter A. Ercius, Jordan S. Pierce, and Benjamin J. McMorran. Aberration corrected STEM by means of diffraction gratings. *Ultramicroscopy*, 182:36–43, November 2017.

[69] Roy Shiloh, Roei Remez, Peng-Han Lu, Lei Jin, Yossi Lereah, Amir H. Tavabi, Rafal E. Dunin-Borkowski, and Ady Arie. Spherical aberration correction in a scanning transmission electron microscope using a sculpted thin film. *Ultramicroscopy*, 189:46–53, June 2018.

[70] Tyler R Harvey, Fehmi S Yasin, Jordan J Chess, Jordan S Pierce, Roberto M. S. dos Reis, Vasfi Burak Özdöl, Peter Ercius, Jim Ciston, Wenchun Feng, Nicholas A. Kotov, Benjamin J McMorran, and Colin Ophus. Interpretable and efficient contrast in scanning transmission electron microscopy with a diffraction grating beamsplitter. *arXiv:1808.00370 [physics.ins-det]*, 2018.

[71] H. Lichte, K.-H. Herrmann, and F. Lenz. Electron noise in off-axis image plane holography. *Optik*, 77(3):135–140, 1987.

[72] W.J. de Ruijter and J.K. Weiss. Detection limits in quantitative off-axis electron holography. *Ultramicroscopy*, 50(3):269–283, 1993.

[73] A. Harcher and H. Lichte. Experimental study of amplitude and phase detection limits in electron holography. *Ultramicroscopy*, 64:57–66, 1996.

[74] L. Marton, J. Arol Simpson, and J. A. Suddeth. Electron beam interferometer. *Physical Review*, 90(3):490–491, 1953.

[75] G. Matteucci and G. Pozzi. A ”mixed” type electron interferometer. *Ultramicroscopy*, 5:219–222, 1979.

[76] Toshiaki Tanigaki, Shinji Aizawa, Hyun Soon Park, Tsuyoshi Matsuda, Ken Harada, and Daisuke Shindo. Advanced split-illumination electron holography without Fresnel fringes. *Ultramicroscopy*, 137:7–11, February 2014.

[77] Toshiaki Tanigaki, Kuniaki Sato, Zentaro Akase, Shinji Aizawa, Hyun Soon Park, Tsuyoshi Matsuda, Yasukazu Murakami, Daisuke Shindo, and Hiromitsu Kawase. Split-illumination electron holography for improved evaluation of electrostatic potential associated with electrophotography. *Applied Physics Letters*, 104(13):131601, March 2014.

[78] Q. Ru, N. Osakabe, J. Endo, and A. Tonomura. Electron holography available in a non-biprism transmission electron microscope. *Ultramicroscopy*, 53:1–7, 1993.

[79] Ben McMorran and Alexander Cronin. Model for partial coherence and wavefront curvature in grating interferometers. *Physical Review A*, 78(1):013601, July 2008.

[80] Adam Caprez, Roger Bach, Scot McGregor, and Herman Batelaan. A wide-angle electron grating bi-prism beam splitter. *Journal of Physics B: Atomic, Molecular and Optical Physics*, 42(16):165503, 2009.

[81] T.R. Harvey, F.S. Yasin, J.J. Chess, J.S. Pierce, R. dos Reis, P. Özdöl, V.B.and Ercius, J. Ciston, W. Feng, N.A. Kotov, B.J. McMorran, and C. Ophus. Interpretable and efficient contrast in scanning transmission electron microscopy with a diffraction grating beamsplitter. *arXiv:1808.00370 [physics.ins-det]*, 2018.

[82] Fehmi S. Yasin, Tyler R. Harvey, Jordan J. Chess, Jordan S. Pierce, Colin Ophus, Peter Ercius, and Benjamin J. McMorran. Probing light atoms at subnanometer resolution: Realization of scanning transmission electron microscope holography. *Nano Letters*, 0(0):null, 2018. PMID: 30265544.

[83] Roy Shiloh, Roei Remez, Peng-Han Lu, Lei Jin, Yossi Lereah, Amir H. Tavabi, Rafal E. Dunin-Borkowski, and Ady Arie. Spherical aberration correction in a scanning transmission electron microscope using a sculpted thin film. *Ultramicroscopy*, 189:46 – 53, 2018.

[84] T Ohnishi, H Koike, S Tomimatsu, K Umemura, and T Kamino. A new focused-ion-beam microsampling technique for tem observation of site-specific areas. *Proceedings of the 25th International Symposium on Testing and Failure Analysis*, pages 449–453, 1999.

[85] Stephan Uhlemann, Heiko Müller, Peter Hartel, Joachim Zach, and Max. Haider. Thermal Magnetic Field Noise Limits Resolution in Transmission Electron Microscopy. *Physical Review Letters*, 111(4):046101, July 2013.

[86] Robert C. Forrey, A. Dalgarno, and Jrg Schmiedmayer. Determining the electron forward-scattering amplitude using electron interferometry. *Physical Review A*, 59(2):R942–R945, 1999.

[87] Y. Aharonov and D. Bohm. Significance of electromagnetic potentials in the quantum theory. *Physical Review*, 115(3):485–491, August 1959.

[88] Gerald Badurek, Harald Weinfurter, Roland Ghler, Achim Kollmar, Stefan Wehinger, and Anton Zeilinger. Nondispersive phase of the aharonov-bohm effect. *Physical Review Letters*, 71(3):307–311, 1993.

[89] Meri Özcan. Influence of electric potentials on atom interferometers: Increased rotation sensitivity. *Journal of Applied Physics*, 83(11):6185–6186, 1998.

[90] Jo Verbeeck, Armand Béché, Knut Müller-Caspary, Giulio Guzzinati, Minh Anh Luong, and Martien Den Hertog. Demonstration of a 2x2 programmable phase plate for electrons. *Ultramicroscopy*, 190:58–65, July 2018.

[91] Vincenzo Grillo, Tyler R. Harvey, Federico Venturi, Jordan S. Pierce, Roberto Balboni, Frdric Bouchard, Gian Carlo Gazzadi, Stefano Frabboni, Amir H. Tavabi, Zi-An Li, Rafal E. Dunin-Borkowski, Robert W. Boyd, Benjamin J. McMorran, and Ebrahim Karimi. Observation of nanoscale magnetic fields using twisted electron beams. *Nature Communications*, 8(1):689, September 2017.

[92] Ludwig Reimer and Helmut Kohl. *Transmission Electron Microscopy: Physics of Image Formation*. Springer, 2008. 00020.

[93] Daisuke Shindo and Yasukazu Murakami. Electron holography of magnetic materials. *Journal of Physics D: Applied Physics*, 41(18):183002, 2008.